

Unified Theory of Thermal Quenching in Inorganic Phosphors

Mahdi Amachraa^{a†}, Zhenbin Wang^{b†}, Chi Chen^b, Shruti Hariyani^c, Hanmei Tang^a, Jakoah Brgoch^c, Shyue Ping Ong^{b*}

^aMaterials Science and Engineering Program, University of California San Diego, 9500 Gilman Dr, Mail Code 0418, La Jolla, CA 92093-0448, United States

^bDepartment of NanoEngineering, University of California San Diego, 9500 Gilman Dr, Mail Code 0448, La Jolla, CA 92093-0448, United States

^cDepartment of Chemistry, University of Houston, College of Natural Sciences and Mathematics, Fleming Building, Room 112, Houston, Texas 77204-5008

Abstract: We unify two prevailing theories of thermal quenching (TQ) in rare-earth-activated inorganic phosphors – the cross-over and thermal ionization mechanisms – into a single predictive model. Crucially, we have developed computable descriptors for local activator environment stability from *ab initio* molecular dynamics simulations to predict TQ under the cross-over mechanism, which can be augmented by a band gap calculation to account for thermal ionization. The resulting TQ model predicts the experimental TQ in 29 known phosphors to within ~3-8%. Finally, we have developed an efficient topological approach to rapidly screen vast chemical spaces for the discovery of novel, thermally robust phosphors.

INTRODUCTION

Lighting accounts for approximately 15% of global energy consumption and 5% of CO₂ emissions.¹ Solid-state lighting (SSL), based on phosphor-converted light-emitting diodes (pc-LEDs), is ~10x more efficient than traditional lighting and therefore offers a huge opportunity to achieve substantial energy savings and CO₂ reductions. A critical component in pc-LEDs is the rare-earth substituted inorganic phosphor, which down-converts the near-ultraviolet or blue LED emission to longer wavelengths. The phosphors currently employed in these bulbs comprise an inorganic host material, such as an oxide or nitride, activated with a rare-earth ion that is typically Ce³⁺ or Eu²⁺. The prototypical phosphor used in a majority of devices is yttrium aluminum garnet, Y₃Al₅O₁₂, activated with Ce³⁺ (YAG:Ce³⁺) to produce a bright yellow emission. Exciting this phosphor when it is coated on top of a blue LED chip produces a broad emission across the visible spectrum light, appearing as white light.

Developing phosphors with high quantum efficiency and excellent thermal stability is a long-standing quest within the SSL community. Emission loss with increasing temperature (also known as thermal quenching or TQ) is of particular importance in next-generation SSL, where high-power LEDs and laser-based LEDs are becoming more common. In combination with smaller device packaging, the heat generated in these devices can negatively influence the optical output, in particular from the phosphor.² The TQ of a phosphor is experimentally determined by taking the ratio between the integrated light intensity emitted at operating temperature (~423–473 K) and the integrated intensity of light emitted at room temperature. Commercial phosphors, such as YAG:Ce³⁺, have a TQ of less than 10%, meaning a majority of the emission intensity is maintained at high temperature, whereas other phosphors can be entirely thermally quenched (TQ = 100%) at high temperature. It is therefore unsurprising that extensive efforts have been devoted to the investigation of the TQ mechanism in phosphors.^{3–6}

Two dominant theories have been proposed to explain the TQ behavior in Ce³⁺ and Eu²⁺-activated phosphors. In the 1960s, Blasse *et al.* proposed that TQ is the result of the non-radiative relaxation of electrons from the excited state to the ground state.^{7,8} This “cross-over” mechanism is represented schematically using the configurational coordinate diagram in Figure 1, where the energy difference between the relaxed excited state and the cross-over point E_a^{co} determines the activation barrier for this process. This theory is one of the reasons why there is a search for structurally rigid phosphor hosts. The fundamental assumption here is that a more rigid host prevents access to soft phonon modes, reducing the probability of non-radiative relaxation from the excited configuration to the ground state configuration. However, subsequent experiments have found many violations of this relationship; for example, the Ca₇Mg(SiO₄)₄:Eu²⁺, CaMgSi₂O₆:Eu²⁺, and Sr₆M₂Al₄O₁₅:Eu²⁺ (M = Y, Lu, Sc) phosphors all suffer from TQ despite their seemingly rigid crystal structures, as estimated from their comparatively high Debye temperatures.^{9,10} The second theory, attributed to Dorenbos, posits that TQ is due to the thermal excitation of the excited 5*d* electron of Ce³⁺/Eu²⁺ to the conduction band of the host;⁶ the activation barrier of this thermal ionization process (E_a^i in Figure 1) determines the TQ of a phosphor, and this barrier is in turn correlated to the band gap of the phosphor host.¹¹ Other TQ pathways have been suggested as well, e.g., the temperature dependence of the conduction band minimum is expected to lower E_a^i and induce TQ,³ although the two competing mechanisms (“cross-over” mechanism and thermal ionization process) dominate in the loss of luminescence as a function of temperature in Ce³⁺/Eu²⁺ doped phosphors.

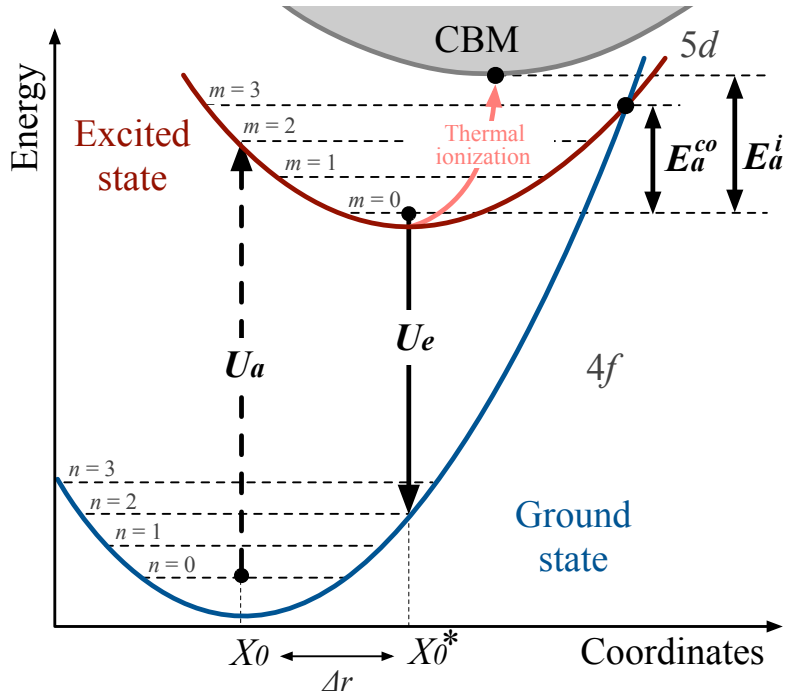


Figure 1. Configurational coordinate diagram for the activator in a phosphor. Excitation is allowed from the vibrational level $n = 0$ of the ground state to the excited state and results in the absorption energy U_a . The relaxation of the system from the vibrational level $m = 0$ to the ground state results in the emission energy U_e . The displacement $\Delta r = X_0^* - X_0$ is the polyhedron average bond length difference between the excited and ground state of the activator. In the cross-over model, thermal quenching results from the non-radiative relaxation of an excited electron to the ground state when the temperature is high enough to overcome the activation energy E_a^{co} . In the Dorenbos thermal ionization model, thermal quenching results from the promotion of excited electrons to the conduction band minimum if the temperature is high enough to overcome the activation energy E_a^i .

In this work, we develop a unified theory of TQ in phosphors by considering the competition between the two dominant TQ mechanisms. It should be noted that all other forms of quenching, thermal or otherwise, are ignored. The focus of this work is specifically on TQ in Ce^{3+} and Eu^{2+} -activated oxide phosphors, which are the most common rare-earth ions employed in phosphors and operate on the highly efficient $4f^n 5d^0 \rightarrow 4f^{n-1} 5d^1$ transition. Using *ab initio* molecular dynamics simulations (AIMD), we establish that the local environment stability around the rare-earth ion as a function of temperature is a robust, transferable descriptor for TQ under the cross-over mechanism when the host band gap is sufficiently large. If the host band gap is small, however, the thermal ionization mechanism competes with the cross-over mechanism. We, therefore, develop a model accounting for both quenching mechanisms to predict the TQ of known phosphors. A total of 29 oxide phosphors with experimentally-measured TQ values were selected to construct the models. Information on these phosphors is summarized in Table S1. Our results show that the combination of AIMD simulations and band gap (E_g) calculations provides a clear relationship between a series of computed descriptors and a phosphor's thermal quenching behavior. Furthermore, we propose a novel topological descriptor based on the Voronoi analysis that can be used to rapidly screen for low TQ phosphors without expensive AIMD simulations, thereby allowing the discovery of new thermally robust inorganic phosphors.

METHODS

Density Functional Theory (DFT) calculations. All DFT calculations were performed using the Vienna *ab initio* simulation package (VASP) within the projector-augmented wave method.^{12,13} The exchange-correlation interaction was described using the Perdew-Berke-Ernzerhof (PBE)¹⁴ generalized gradient approximation (GGA) functional with the Hubbard U extension. In general, the parameters used are similar to those used in the Materials Project¹⁵, with a plane wave energy cutoff of 520 eV and a k -point density at least of 100 per \AA^{-3} . A U value of 2.5 eV was used for the $4f$ orbitals in Eu and Ce following previous works.^{12,16} All structures were fully relaxed with energies, and forces converged to within 10^{-5} eV and 0.01 eV/ \AA , respectively.

To construct the $\text{Ce}^{3+}/\text{Eu}^{2+}$ -activated phosphors, $\text{Ce}^{3+}/\text{Eu}^{2+}$ was doped into all compatible symmetrically distinct sites in supercells of the host crystal with lattice parameters of at least 10 \AA in each direction. The lowest energy $\text{Ce}^{3+}/\text{Eu}^{2+}$ -doped structure was then used for subsequent analysis and AIMD simulations. All crystal structure and data analysis were carried out using the Python Materials Genomics (pymatgen) package.¹⁷

Ab initio molecular dynamics (AIMD) simulations. AIMD simulations were carried out on the supercell models of $\text{Ce}^{3+}/\text{Eu}^{2+}$ -activated phosphors in the NVT ensemble at 300 K and 500 K with a Nose-Hoover thermostat.¹⁸ The simulation cell was fixed at the final 0 K relaxed cell parameters for each phosphor. For reasons of computational efficiency, the AIMD simulations were non-spin-

polarized, and a minimal Γ -centered $1 \times 1 \times 1$ k -point mesh and a time step of 2 fs were adopted. Given that the main output extracted from the AIMD simulations is the local environment fluctuations, we expect this approximation to be reasonable.

Host Debye temperature calculations. The Debye temperatures of all host compounds were calculated using the quasi-harmonic model given by:

$$\Theta_D = \frac{h}{2\pi k_B} \left(6\pi^2 V^{\frac{1}{3}} n \right) f(v) \sqrt{\frac{B}{M}}$$

where, V , n , $f(v)$, V and M are the unit cell volume, the number of atoms in the unit cell, a scaling function in terms of Poisson's ratio ν , the bulk modulus and the molar mass, respectively; h and k_B refer to the Planck's constant, and the Boltzmann constant, respectively.¹⁹

Activator local environment determination. The local environments of the activator ions were computed using the algorithm of Waroquiers *et al.* implemented in pymatgen.²⁰ Additionally, Hoppe's effective coordination number (ECoN) was utilized to determine bond weight based on geometry, leading to a chemically guided local environment algorithm.²¹ Based on the polyhedron geometry with the highest weight, a unique cut-off radius or maximum distance factor (MDF) was determined and used to determine the local environment distribution changes during AIMD simulations. The MDF α was computed as follows:

$$\alpha = \frac{l^x}{l_{min}^x}$$

where l^x and l_{min}^x are the ligand-activator bond length and the smallest activator-ligand bond length, respectively, and the ECoN values were computed as follows:

$$\begin{aligned} \text{ECoN} &= \sum \exp\left(1 - \left(\frac{l_i}{l_{avg}}\right)^6\right) \\ l_{avg} &= \frac{\sum(l_i \exp\left(1 - \left(\frac{l_i}{l_{min}}\right)^6\right))}{\sum(\exp\left(1 - \left(\frac{l_i}{l_{min}}\right)^6\right))} \end{aligned} \quad (1)$$

l_i , l_{min} , and l_{avg} are the ligand-activator bond length, the lowest ligand-activator bond length, and the weighted average bond length, respectively.

The Voronoi representation computes a polar transformation of an activator's nearest neighbors into a Cartesian frame and requires an additional angular parameter:

$$\gamma = \frac{\theta^x}{\theta_{max}^x}$$

θ_{max}^x and θ^x are the widest angle to uniquely define a given set of ligands and the angle at which the local environment is considered, respectively.

Average cation electronegativity and centroid shift. The centroid shift, ε_c , was expressed by Dorenbos²² as follows:

$$\varepsilon_c = \frac{1.44 \times 10^{17} \alpha_{sp} N_a}{R_{eff}^6}$$

where, α_{sp} is the effective spectroscopic polarizability, which for oxides is given as²³ $\alpha_{sp} = 0.4 + \frac{4.6}{\chi_{av}^2}$, where, χ_{av} is defined as the average cation electronegativity;²⁴ N_a is the number of anions in the first surrounding shell and R_{eff} is the effective bond length estimated as:

$$R_{eff} = \frac{1}{N_a} \sum_{i=1}^{N_a} (R_i - 0.6\Delta R)$$

where R_i are the bond lengths between the activator ($\text{Ce}^{3+}/\text{Eu}^{2+}$) site to the ligands in the host structure, and ΔR accounts for the difference in ionic radius between the activator and the cation it substitutes for. In this work, R_{eff} and N_a are replaced with Hoppe's l_{avg} (equation 1) and ECoN, respectively, computed using the DFT-relaxed phosphor structures containing the rare-earth ion, leading to the following expression for the centroid shift:

$$\varepsilon_c^{DFT} = \frac{1.44 \times 10^{17} \alpha_{sp} \text{ECoN}}{l_{avg}^6} \quad (2)$$

Estimation of the crystal field splitting. The point charge electrostatic model (PCEM)²⁵ provides the most straightforward geometrically-driven approach to describe ε_{cfs} in terms of crystal field parameters denoted by B_q^k ; where k and q values depend on the point group symmetry of the centroid's polyhedron. The B_q^k parameters are defined as the product of two independent components: a radial part $f(R)$ and an angular part Θ_q^k . Although the PCEM is not well suited for computing accurate ε_{cfs} values, it has been previously established that there is a positive correlation between the fourth-rank angular parameter (Θ_q^4), R_{eff}^{-2} , and ε_{cfs} in Ce^{3+} -doped phosphors in the octahedral, cubic, tricapped trigonal prismatic, and cuboctahedron geometries, given by:

$$\varepsilon_{cfs}(R) = \beta_{poly} R_{eff}^{-2}$$

where β_{poly} is the shape factor and is dependent on the polyhedron geometry and correlated to the angular part Θ_q^4 , while R_{eff}^{-2} accounts for the radial part of ϵ_{cfs} .²² The general PCEM expression for the B_0^2 , and B_0^4 crystal field parameters have the form:

$$B_0^2 = f(R) \Theta_0^2 = Ze^2 \frac{\langle r^2 \rangle}{R_{eff}^3} \left[p - \frac{n}{2} + m(3 \cos^2(\theta_{pr}) - 1) \right]$$

$$B_0^4 = f(R) \Theta_0^4 = Ze^2 \frac{\langle r^4 \rangle}{R_{eff}^5} \left[p + \frac{3n}{8} + \frac{m}{4} (35 \cos(\theta_{pr})^4 - 30 \cos(\theta_{pr})^2 + 3) \right]$$

where, Ze is the effective charge on the ligands (oxygen in this study) separated by a distance R_{eff} from the centroid (Ce^{3+}/Eu^{2+}), r^2 or r^4 is the expectation value of the radial distance to the of the $5d$ orbital from the nucleus second or fourth power and its value is assumed to be constant, p is the number of axial ligands, n is the number of equatorial ligands, m is the number of ligands in the base plane of the prism, and θ_{pr} is the prismatic angle between the $2m$ prismatic ligands and the m -fold rotational axis. Three types of activator geometries are found within the Ce^{3+} -doped phosphors considered in this study, namely, cubic, octahedral and trigonal prismatic with point groups O_h , O_h , and D_{3h} , respectively (see Figure 2). Both the O_h and D_{3h} point groups can be defined under a 3-fold rotation axis. The cubic and octahedral geometries share the same 3-fold rotational axis with the following Θ_0^2 , and Θ_0^4 values:

$$\Theta_0^2(\text{oct}) = 0; \Theta_0^4(\text{oct}) = -2.33$$

$$\Theta_0^2(\text{cub}) = 0; \Theta_0^4(\text{cub}) = 2.07$$

$\Theta_0^4(\text{oct})$ has a negative value, i.e., the e_{2g} orbitals in an octahedral environment experience repulsive forces, while $\Theta_0^4(\text{cub})$ has a positive value, and the e_{2g} orbitals in a cubic environment experience high attractive forces. For the trigonal prismatic with a D_{3h} symmetry, ($\theta_{pr} = 49^\circ$, $m = 3$, $CN = 6$) the PCEM values for Θ_0^2 and Θ_0^4 can be extracted as follows:

$$\Theta_0^2 = m[3 \cos^2(\theta_{pr}) - 1] = 0.87$$

$$\Theta_0^4 = m \frac{m}{4} [(35 \cos(\theta_{pr})^4 - 30 \cos(\theta_{pr})^2 + 3)] = -2.57$$

The polyhedron geometries around the Eu^{2+} considered in the study generally exhibit complex geometries defined under different rotational axis. In this work, we utilize Hoppe's effective coordination to identify the highest weight bonds, which are likely to have the highest effect on the ϵ_{cfs} , followed by Waroquiers *et al.*'s algorithm to identify all possible symmetries an activator's polyhedron can have with respect to small local atomic displacements (see Figure S1 for a flowchart). The 18 Eu^{2+} local environments in this study are then classified into four distinct geometries: D_{3h} trigonal prism, O_h octahedron, C_{2v} mono-capped or bi-capped trigonal prism (1CTP or 2CTP), and I_h icosahedron. In this work, we assume that the crystal field splitting of a mono-capped trigonal prism is comparable to other crystal field splitting when defined under a 3-fold rotation axis, as suggested by previous results.²⁶ The bi-capped trigonal prism is approximated as a mono-capped trigonal prism. Therefore, for the mono/bi-capped trigonal prism with a C_{2v} symmetry, ($\theta_{pr} \sim 47^\circ$, $p = 0$, $n = 1$, $m = 3$, $CN = 7$) the PCEM values for Θ_0^2 and Θ_0^4 can be extracted as follows:

$$\Theta_0^2(1CTP) = 0.69; \Theta_0^4(1CTP) = -2.16$$

The icosahedron with I_h symmetry possesses a 5-fold rotation axis, which is not compatible with its crystallographic space group; hence only distorted icosahedra are allowed to occur in real crystals, where the second and fourth-rank parameters are equal to zero in both the 5-fold and 3-fold rotation axis.²⁵ The local environment approximations considered in this work are essential to defining all crystal-field parameters under a unique quantization axis (3-fold), ensuring the direct comparison of all computed parameters.

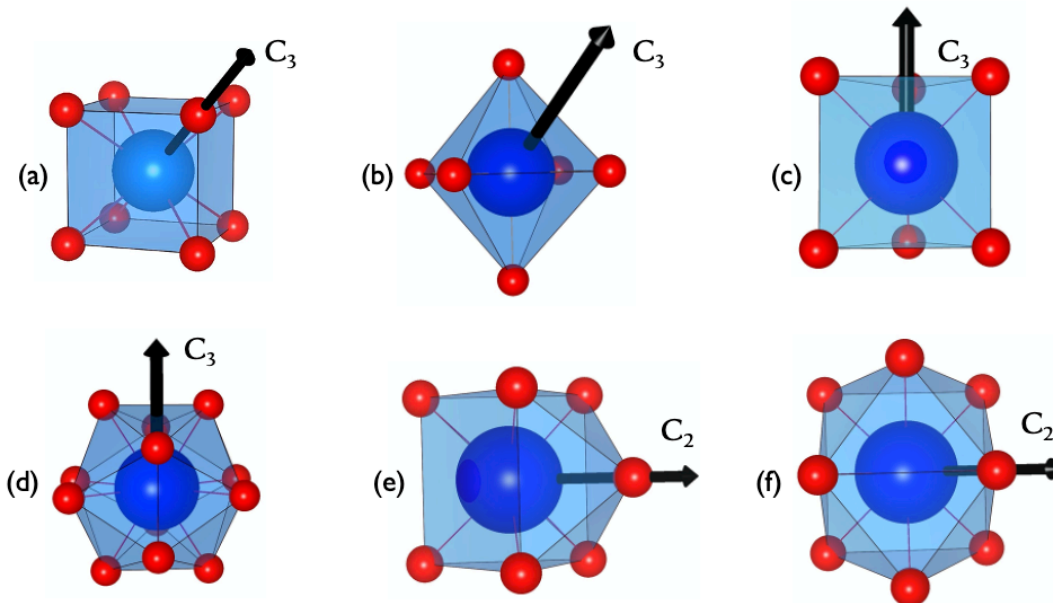
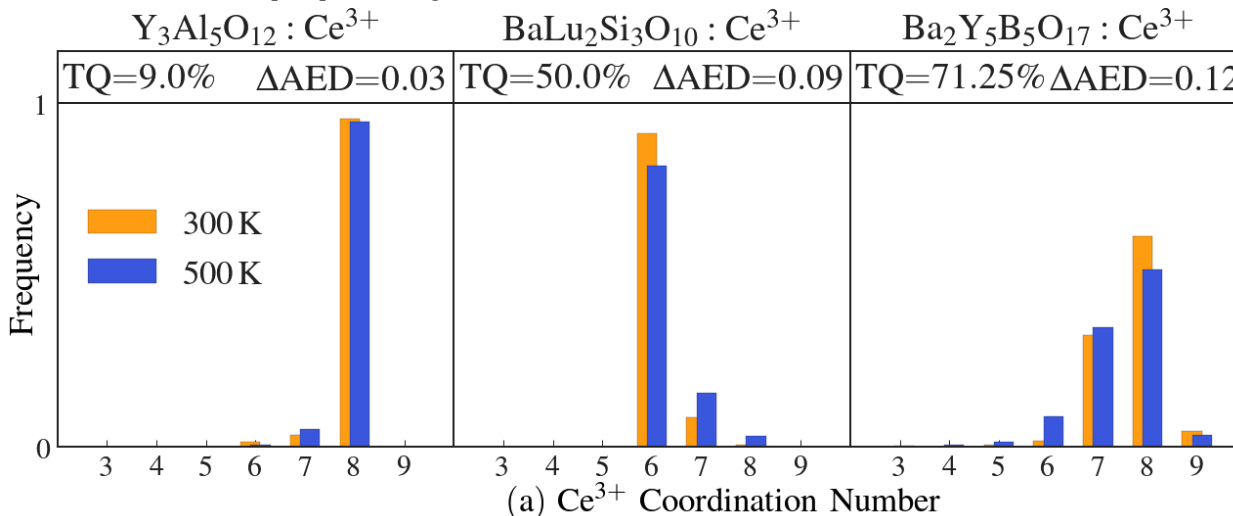


Figure 2. Local environments in the 29 $\text{Ce}^{3+}/\text{Eu}^{2+}$ -doped phosphors: (a) cube (O_h), (b) octahedron (O_h), (c) trigonal prism (D_{3h}), (d) icosahedron (I_h), (e) mono-capped trigonal prism (C_{2v}), and (f) bi-capped trigonal prism (C_{2v}). C_3 and C_2 refers to the rotational axis. It should be noted that the local environments shown here are the idealized coordination polyhedra (without distortion). Actual local environments in the phosphors may be distorted from these idealized shapes.

RESULTS AND DISCUSSION

Relationship between Thermal Quenching and Local Environment Rigidity

AIMD simulations were performed on the 29 phosphors at room temperature (300 K) as well as 500 K to represent an upper-temperature limit experienced by the phosphor during lamp operation.²⁷ An activator environment distribution (AED) at both temperatures was constructed for each phosphor from the AIMD trajectories. The AED is derived by determining the number of simulation timesteps that the activator has a particular coordination number (CN) using the algorithm developed by Waroquier *et al.*,²⁰ normalized across the total number of timesteps. Figure 3 presents the AED for three Ce^{3+} and three Eu^{2+} -activated phosphors with high (> 80%), intermediate (40-60%) and low (< 20%) TQ. Similar plots for the remaining 23 phosphors are provided in Figures S2 and S3. Comparing the AEDs between 300 K and 500 K show that thermally robust (small TQ) phosphors generally exhibit minimal change in the AED as a function of temperature whereas thermally quenched (high TQ) phosphors show substantial shifts in the AED with temperature. For example, the Ce^{3+} in $\text{YAG}:\text{Ce}^{3+}$ (TQ = 9%) is primarily eight-fold coordinated with oxygen and its CN remains stable at 500 K. In contrast, the Ce^{3+} in $\text{Ba}_2\text{Y}_3\text{B}_5\text{O}_{17}:\text{Ce}^{3+}$ (TQ = 71%) has a distribution of CN of 7-8 at 300 K and exhibits an obvious shift to lower CNs, including seven-fold and six-fold coordination environments, at 500 K. The same trend is observed for Eu^{2+} -activated phosphors in Figure 3b.



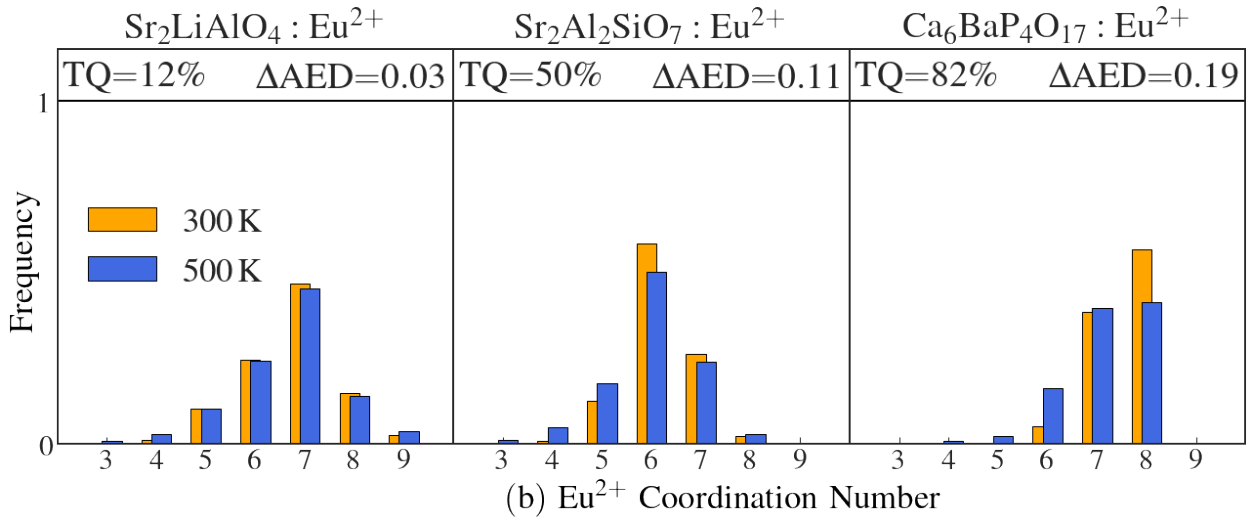


Figure 3. Activator environment distribution (AED). The computed AED of (a) Ce^{3+} and (b) Eu^{2+} at 300 K and 500 K in three hosts with distinct TQ behaviors. The experimental TQ values were obtained from references^{28–36}

To quantify the shift in the AED from 300 K to 500 K, we define ΔAED as the Euclidean distance between AEDs at 300 K and 500 K in Equation 3,

$$\Delta\text{AED} = \sqrt{\sum_{x=2}^{12} (\omega_{\text{CN}=x}^{300\text{K}} - \omega_{\text{CN}=x}^{500\text{K}})^2} \quad (3)$$

where $\omega_{\text{CN}=x}^{300\text{K}}$ and $\omega_{\text{CN}=x}^{500\text{K}}$ are the normalized CN frequencies at 300 K and 500 K, respectively, and the CN ranges from 2 to 12. Figure 4 shows the experimentally measured TQ (TQ_{exp}) plotted against the computed ΔAED for Ce^{3+} and Eu^{2+} -activated phosphors. We find there is an approximately-linear positive correlation between TQ and ΔAED for both Ce^{3+} and Eu^{2+} -activated oxide phosphors. A least-squares fitting for the one-parameter expression $\text{TQ} = K\Delta\text{AED}$, where K is a constant, yields R^2 values of 0.89 and 0.62 for Ce^{3+} and Eu^{2+} -activated phosphors, respectively, with reasonable root mean square errors (RMSEs) of 11.6% and 14.3%, respectively. In contrast, the DFT-calculated Debye temperature (Θ_D) yields a weaker correlation against TQ_{exp} (see Figure S4) with R^2 values of 0.14 and 0.12 for Ce^{3+} and Eu^{2+} -activated phosphors, respectively, and corresponding RMSEs of 32% and 26%, respectively. There is some correlation between ΔAED and host structural rigidity, as suggested by the high Debye temperatures, the coordinated local displacements within a crystal environment are more directly related to the low ΔAED , making it more reliable compared to a global descriptor like structural rigidity. These observations support our hypothesis that ΔAED is an effective descriptor to probe the depth of the potential energy surface (PES) in the cross-over model, where a higher ΔAED implies a shallower PES in the ground and excited states, which results in a lower E_a^{co} and higher TQ.

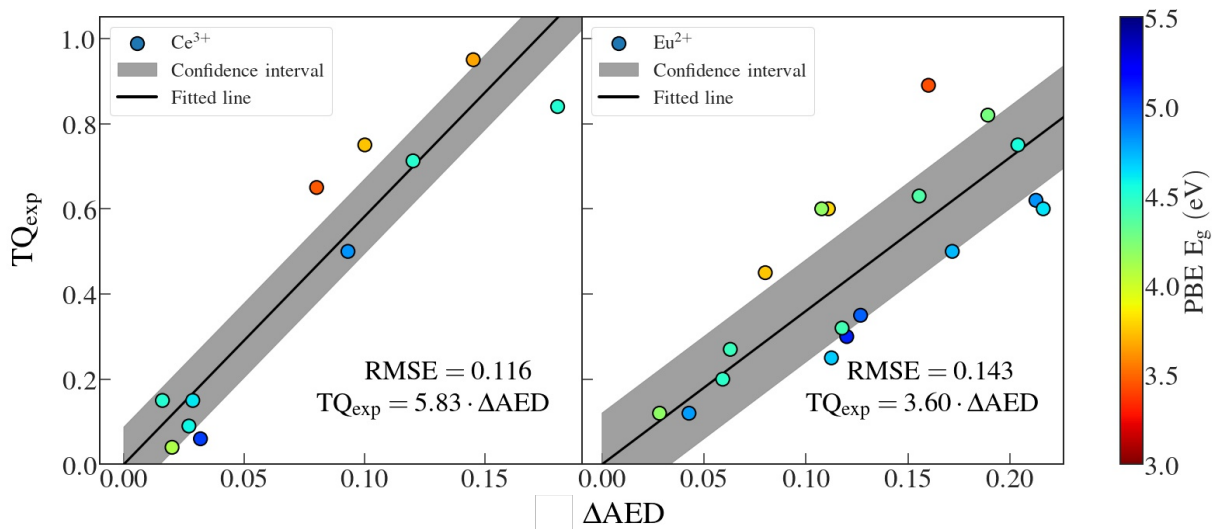


Figure 4. Local environment rigidity. Plot of experimental thermal quenching (TQ_{exp}) against the change in the activator environment distribution (ΔAED) for Ce^{3+} (left), Eu^{2+} (right) activated phosphors. The marker colors are based on their calculated band gap using the Perdew-Burke-Ernzerhof (PBE) functional (see color bar). The root mean square error (RMSE) for each model is defined as the

square root of the average squared difference between the computed ΔAED and the experimental TQ (TQ_{exp}), i.e. $RMSE =$

$$\sqrt{\frac{1}{N} \sum_{i=1}^N (TQ_{\text{exp}}^i - K\Delta AED^i)^2}.$$

Accounting for Thermal Ionization

A closer examination of Figure 4 further reveals that phosphors with large host band gaps (E_g) lie below the regression line, and those with small E_g lie above the line. This observation suggests that E_g , which is related to TQ under the Dorenbos single-barrier quenching model, also plays a critical role for some materials.

Figure 5 shows a schematic of the energy levels of a Ce^{3+}/Eu^{2+} activator in a host. It can be seen that the Dorenbos thermal ionization barrier is given by:

$$E_a^i(A^{x+}, H) = E_g - \left[E(A^{x+}, \text{free}) - \varepsilon_c(A^{x+}, H) - \frac{\varepsilon_{cfs}(A^{x+}, H)}{r(H)} + \varepsilon_s(A^{x+}, \text{free}) \right] - E(4f^n - \text{VBM}) \quad (4)$$

where, E_g is the band gap of the host, $E(A^{x+}, \text{free})$ is the fixed centroid position for the free A^{x+} ion ($E(Ce^{3+}, \text{free}) = 6.118$ eV and $E(Eu^{2+}, \text{free}) = 4.216$ eV),³⁷ $\varepsilon_c(A^{x+}, H)$ is the centroid shift for A^{x+} in the host H, $\varepsilon_{cfs}(A^{x+}, H)$ is the crystal-field splitting experienced in the host H, $r(H)$ expresses the ratio between the crystal field splitting and the crystal field shift (typical values range between 1.7 and 2.4 and are geometry dependent), $\varepsilon_s(A^{x+}, \text{free})$ is the energy difference between the centroid position and the lowest $5d$ level of the free A^{x+} ion and is also a constant, and $E(4f^n - \text{VBM})$ is the energy difference between the $4f^n$ of A^{x+} and the valence band maximum (VBM) of the host H. The binding energy $E(4f^n)$ for Ce^{3+} has been found to be relatively constant for garnets and perovskites and will be assumed constant for the 11 Ce^{3+} -doped hosts considered in the study, while $E(4f^n)$ for Eu^{2+} has an energy fluctuation of ~ 0.38 eV in oxides depending on the host H.²² The $r(H)$ is assumed $5/2$ for 6-coordinated geometries, and $5/3$ for 8-coordinated geometries.²⁵ The $\varepsilon_c(Ce^{3+}, H)$ was evaluated using the ligand polarization model where the spectroscopic polarizability is quantitatively correlated to χ_{av} as defined in the Methods section. Finally, the susceptibility of the $5d$ energy levels induces an additional redshift, namely, the crystal field splitting $\varepsilon_{cfs}(A^{x+}, H)$, which can be determined by the geometry around the Ce^{3+}/Eu^{2+} activators as outlined in the Methods section. For brevity, we will drop the explicit functional dependence of the variable henceforth.

Based on equation 4, we, therefore, express the thermal ionization barrier as follows:

$$E_a^i = AE_g^{DFT} + B\varepsilon_c^{DFT} + \frac{1}{r} \left(C \frac{\Theta_0^2}{l_{avg}^3} + D \frac{\Theta_0^4}{l_{avg}^5} \right) + E \quad (5)$$

where ε_{cfs} is expressed as the sum of both second and fourth-rank crystal-field parameters:

$$\varepsilon_{cfs} = C \frac{\Theta_0^2}{l_{avg}^3} + D \frac{\Theta_0^4}{l_{avg}^5}$$

where A, B, C, D and E are fitted constants. A accounts for the well-known systematic underestimation of E_g by the PBE functional,³⁸ while B accounts for systematic errors in the estimation of the centroid shift from the DFT lattice parameters (Equations 1 and 2). C and D constants account for the mutual importance of the second and fourth-rank crystal-field parameters, as well as the refactoring of the computed ε_{cfs} energies with respect to the computed E_g^{DFT} and ε_c^{DFT} .

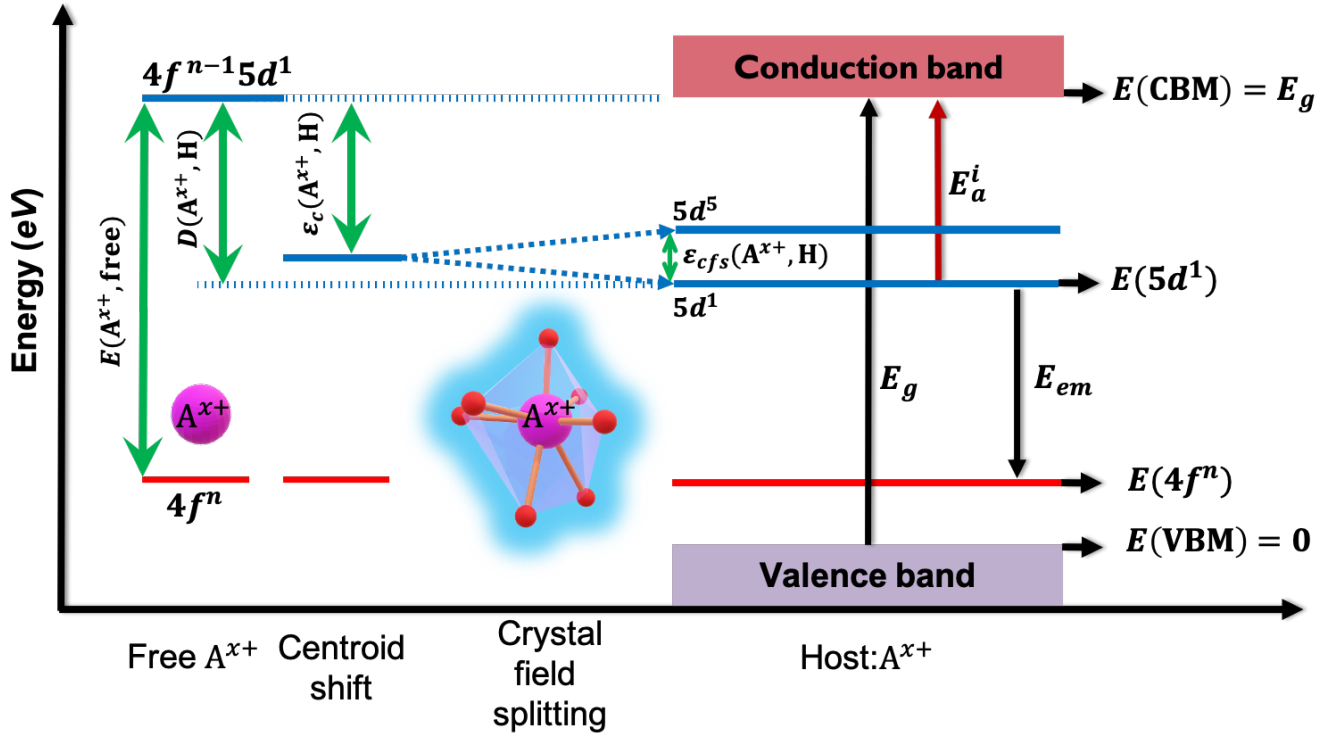


Figure 5. Energy level diagram for $\text{Ce}^{3+}/\text{Eu}^{2+}$ activators (denoted by A^{x+}) in a host material (denoted by H). The $\epsilon_c(\text{A}^{x+}, \text{H})$, $\epsilon_{cfs}(\text{A}^{x+}, \text{H})$, $D(\text{A}^{x+}, \text{H})$ and $E(\text{A}^{x+}, \text{free})$ refer to the centroid shift, crystal-field splitting, the redshift of the activators' $4f^{n-1}5d^1$ level in a host H, respectively, and the energy of the first $f \rightarrow d$ transition the free ion A^{x+} . The VBM and the CBM indicate the valence band maximum and the conduction band minimum, respectively. Note that the energy of the VBM is the energy referential and is set to 0 eV.

Considering the cross-over model and the thermal ionization model for quenching are two independent sources of TQ, both are likely occurring simultaneously in some phosphor systems. Therefore, we combine ΔAED with the Dorenbos expression for TQ⁶ under the thermal ionization model (detailed derivations are provided in Supporting Information) to arrive at the following formula of TQ_{pred}:

$$\text{TQ} = 1 - (1 - K\Delta\text{AED}) \frac{1 + \Gamma e^{\frac{-E_a^i}{k_B T_1}}}{1 + \Gamma e^{\frac{-E_a^i}{k_B T_2}}} \quad (6)$$

where, k_B is the Boltzmann constant, T_1 (300 K) is the initial temperature in Kelvin, T_2 is the final temperature of quenching, which in these calculations is 500 K, Γ is defined as the ratio of the attempt rate for thermal quenching (Γ_0) and the radiative decay rate of the $5d$ state (Γ_r)^{6,28}, and E_a^i is the barrier for thermal ionization under the Dorenbos model.

Table 1. Optimized coefficients from non-linear least-squared minimization of unified TQ model for Ce^{3+} and Eu^{2+} activated hosts.

Activator	A	B	C	D	E	K	K'	β
Ce^{3+}	0.15	0.15	0.13	0.037	0.180 eV	4.05	0.27	2.75
Eu^{2+}	0.19	0.012	0.21	0.41	0.049 eV	3.22	0.77	0.86

The optimal values of K , A , B , C , D , and E (as defined in equation 5) were determined by performing a non-linear least-square minimization of the multi-variable predicted TQ from Equation 6 with the experimentally-observed TQ of the 29 phosphors (see Table S1) and are tabulated in Table 1. The Ce^{3+} and Eu^{2+} -activated phosphors are expected to have different A , B , C , D , and E values because of their large difference in energy gap between the $4f$ ground state and the $5d$ excited state (6.2 eV and 4.2 eV for free Ce^{3+} and Eu^{2+} ions, respectively) and different ionic radii.³⁷ Most importantly, the band gap factor ($A=0.15$ and 0.19) for Ce^{3+} and Eu^{2+} is expected to be the same since both are computed using the same functional. Figure 6 plots the predicted TQ_{pred} using the optimized equation 6 against the experimental TQ_{exp}. The RMSE for Ce^{3+} and Eu^{2+} are 3.1% and 7.6%, respectively, which are a significant improvement over the model using ΔAED alone. Further validation of our unified TQ model can be seen in the fact that the predicted E_a^i (Table S1) are in good agreement with experimental thermal ionization energies. For example, the predicted E_a^i of

$\text{Sr}_2\text{MgSi}_2\text{O}_7:\text{Eu}^{2+}$, $\text{SrSc}_2\text{O}_4:\text{Eu}^{2+}$, $\text{Y}_3\text{Al}_5\text{O}_{12}:\text{Ce}^{3+}$, $\text{Lu}_3\text{Al}_5\text{O}_{12}:\text{Ce}^{3+}$ and $\text{K}_3\text{YSi}_2\text{O}_7:\text{Ce}^{3+}$ are 0.87 eV, 0.71 eV, 0.88 eV, 0.87 eV and , 0.54 eV respectively, and the corresponding experimental thermal ionization energies are 0.9 eV, 0.56 eV, 0.77 eV, 0.75 eV and 0.48 eV, respectively.^{22,28,39,40,41} Note, that our predicted E_a^i for $\text{Y}_3\text{Al}_5\text{O}_{12}:\text{Ce}^{3+}$ is higher than the predicted value for $\text{Lu}_3\text{Al}_5\text{O}_{12}:\text{Ce}^{3+}$ as shown in the vacuum referred binding energies diagram.²²

Previous findings from Dorenbos have suggested that the redshift D (the sum of the centroid shift and the crystal splitting shift) of the $5d$ state of the Ce^{3+} activator is correlated to the one of Eu^{2+} ion when inserted within the same host/site as follows:

$$D(\text{Eu}^{2+}, \text{H}) = 0.64D(\text{Ce}^{3+}, \text{H}) - 0.233 \text{ eV} \pm 0.15$$

Equivalently, photoluminescence properties such as emission energy and activation energies of Ce^{3+} -doped phosphors can help assess the photoluminescence of Eu^{2+} when inserted within the same host/site. To further substantiate the validity of our fitted $A, B, C, D,$ and $E,$ we predict the E_a^i of $\text{K}_3\text{YSi}_2\text{O}_7:\text{Eu}^{2+}$ from our fitted results of $\text{K}_3\text{YSi}_2\text{O}_7:\text{Ce}^{3+}$ by utilizing Dorenbos's semi-empirical relationship. The predicted E_a^i of Eu^{2+} doped in $\text{K}_3\text{YSi}_2\text{O}_7$ from the fitted parameters of Ce^{3+} -doped compounds are 0.65 eV, while the experimentally-determined values are 0.63 eV, which are in excellent agreement.

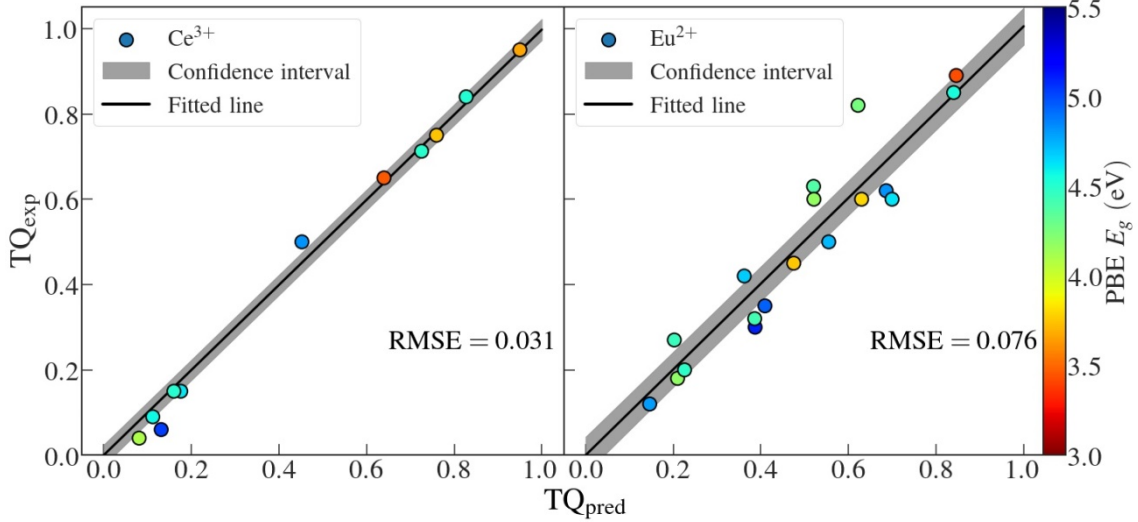


Figure 6. Plot of TQ_{exp} against the predicted TQ (TQ_{pred}) from the unified TQ model (equation 6) for Ce^{3+} (left) and Eu^{2+} (right)-activated hosts. Here, RMSE is computed as follows: $\text{RMSE} = \sqrt{\frac{1}{N} \sum_{i=1}^N (\text{TQ}_{\text{exp}}^i - \text{TQ}_{\text{pred}}^i)^2}$

The unified TQ equation (Equation 6) can be understood intuitively by considering the competition between the cross-over and thermal ionization mechanisms in Figure 1. The primary loss of emission with temperature increase will come from the mechanism with the lowest barrier E_a . When the band gap of the host is large, $E_a^i \gg E_a^{co}$, the cross-over mechanism dominates. ΔAED then describes the depth of the potential energy surface and, hence, TQ. When the band gap of the host is sufficiently small, both mechanisms compete, and $\Delta\text{AED}, E_g, E_g, \epsilon_c,$ and ϵ_{cfs} are required to describe TQ under a dual-barrier quenching model. Unlike the semi-empirical thermal ionization relationship, the proposed unified TQ model allows for the first time to develop a universal comparison amongst all hosts' high temperature photoluminescence behavior *via* robust descriptors ($\Delta\text{AED}, E_g, \epsilon_c, \epsilon_{cfs}$) obtained in a *pre-hoc* manner. Moreover, the E_a^i derived from Dorenbos's semi-empirical relationship is a function of $T_{1/2}$ (the temperature at which the intensity reaches half of the initial intensity), where the latter varies for every host. Consequently, all previously obtained E_a^i mentioned in the literature reflect a thermal quenching occurring across different temperatures ranges, and hence cross-comparisons of E_a^i was impossible and impractical until now. Finally, while the proposed dual-barrier thermal quenching offers a comprehensive overview of the TQ mechanism, its applicability cannot directly be extended to phosphors with multiple luminescent centers, as the AED and electronic properties are expected to differ from the pristine structure. Additionally, phosphors known to have photoluminescence compensation mechanisms driven by the formation of thermally activated defect levels are also not within the scope of the dual-barrier quenching model;⁴² however, with enough data, an additive model accounting for the electronic contributions of defects can be derived.

Intrinsic Topological Descriptor of Activator's Stability. Finally, we demonstrate how a modified version of the unified TQ model can be used to computationally screen for low TQ phosphors. While $E_g^{DFT}, \epsilon_c,$ and ϵ_{cfs} can be obtained using relatively inexpensive ground-state DFT computations, ΔAED requires expensive AIMD simulations for activated phosphors, where relatively large supercells of the host crystal are required to simulate the experimental low activator concentration. It is, therefore, desirable to establish an alternative descriptor for local environment stability. The AED at 300 K and 500 K reveals that activators are susceptible to endure local polyhedron changes due to mutual oscillations of the centroid/activator and ligands/oxygen in the first shell. The computed mean-square displacements (MSD) of the activator and oxygen ligands increase from 300 K to 500 K, suggesting that the

overall occupied 3-dimensional space by the activator and ligands increases with temperature. For example, the MSD behavior of Ce^{3+} and oxygen ligands in the first shell in $\text{Ca}_3\text{Sc}_2\text{Si}_3\text{O}_{12}$ host is shown in Figure S5a; a definite increase in the MSD for both Ce^{3+} and oxygen ligands with respect to temperature is observed. Despite large atomic displacements in $\text{Ca}_3\text{Sc}_2\text{Si}_3\text{O}_{12}$ host, the periodic-like oscillations of both Ce^{3+} and oxygen ligands result in a low ΔAED . Conversely, the MSD behavior of Ce^{3+} and oxygen ligands in $\text{Ba}_3\text{Y}_2\text{B}_6\text{O}_{15}$ host (Figure S5b) shows a quasi-random oscillation resulting in a larger ΔAED . The same observations can be made for $\text{SrMgAl}_{10}\text{O}_{17}:\text{Eu}^{2+}$ and $\text{Ba}_2\text{SiO}_4:\text{Eu}^{2+}$. (Figure S5c and S5d) Consequently, smaller ΔAED values, are suspected to be correlated to large 3-dimensional spaces around the activator's effective local environment.

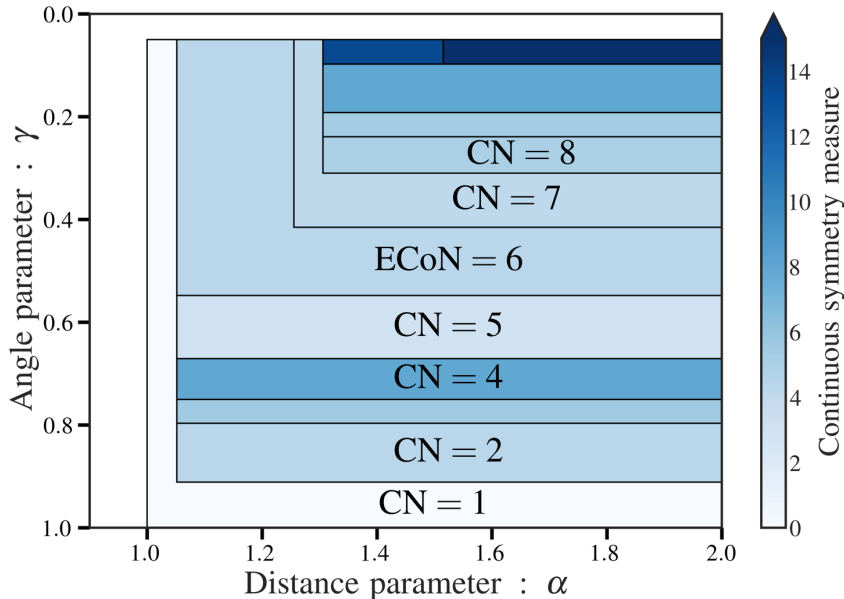


Figure 7. The Voronoi grid representation of Eu^{2+} doped in Sr_2SiO_4 . The Voronoi grid representation has two variables: the angle parameter γ and the distance parameter α . For a specific range of angle and distance parameters, a unique coordination number is defined. Each Voronoi grid is representative of a set of ligands denoted by the coordination number. The continuous symmetry measure is used to assess the degree of symmetry within different coordination numbers and developed by Pinsky.⁴³

A two-dimensional projection of all $\text{Ce}^{3+}/\text{Eu}^{2+}$ local environments in the 29 hosts is constructed via a Voronoi tessellation-based algorithm. Figure 7 shows a *topological* sensitivity analysis of the local activator environment of Eu^{2+} in Sr_2SiO_4 . (similar plots for all of the 29 phosphors are provided in the Supporting Information Figure S6 and S7).^{17,20} By varying the distance (α) and angle (γ) parameters, the algorithm yields different coordination environments due to changes in the bond weights of the surrounding ligands (see Computational Methodology section for bond weights computations). The coordination environment formed by the highest weight ligands determines the main activator local environment, which in $\text{Sr}_2\text{SiO}_4:\text{Eu}^{2+}$ is $\text{ECoN} = 6$. Our hypothesis is that the larger the normalized area (Y) occupied by the main activator local environment, the less sensitive the activator local environment is to variations in bond distances and angles. In other words, the higher Y , the lower the ΔAED , and the smaller the expected TQ. Therefore, substituting ΔAED with $1 - Y$ in equation 7, we obtain the following alternative model:

$$\text{TQ} = 1 - K'(1 - Y) \frac{1 + \Gamma' e^{\frac{-E_a^i}{k_B T_1}}}{1 + \Gamma' e^{\frac{-E_a^i}{k_B T_2}}} \quad (7)$$

where A, B, C, D and E for the E_a^i expression in Equation 5 are kept as the optimized values from the non-linear least-squares optimization of equation 6, while K' is refitted. The optimized values of K' are 0.27 and 0.77 for Ce^{3+} and Eu^{2+} , respectively (included in Table). Moreover, the computed E_a^i from Equation 6 is based on the rate of change of ΔAED across all of the 29 compounds, and ΔAED does not scale linearly with respect to Y . Therefore, to compensate for the different rates of ΔAED and Y , the pre-exponential factor is re-defined as $\Gamma' = \beta\Gamma$. The optimized values of β for Ce^{3+} and Eu^{2+} were 2.75 and 0.86, respectively (shown in Table 1). Figure 8 plots the TQ_{exp} against TQ'_{pred} as defined by equation 7. The RMSE of TQ'_{pred} for Ce^{3+} and Eu^{2+} is 8.9% and 9.6%, respectively. While this value of RMSE is somewhat higher than the RMSE using Equation 6, the RMSE using Equation 7 is already sufficiently low for $\text{Ce}^{3+}/\text{Eu}^{2+}$ -activated hosts to be used for rapid screening for discovery of low TQ phosphors. The difference in performance between using $(1 - Y)$ and ΔAED , especially for Ce^{3+} -activated hosts, can be attributed to two factors. First, some of the considered compounds are known to have multiple symmetrically-distinct doping sites, i.e. $\text{Ba}_3\text{Y}_2\text{B}_6\text{O}_{15}:\text{Ce}^{3+}$, $\text{Ba}_9\text{Lu}_2(\text{SiO}_4)_6:\text{Ce}^{3+}$ and $\text{Ba}_9\text{Lu}_2(\text{SiO}_4)_6:\text{Ce}^{3+}$, while the Voronoi area was computed using only the most energetically stable site.^{32,44} Second, $(1 - Y)$ is a pure topological descriptor with no consideration of differences in chemical bonding, whereas ΔAED captures subtle relationships between bond distances, bond angles and bond strength in the distribution of activator environments.

Nevertheless, the ability to quickly obtain Y values without computationally expensive AIMD calculations makes this approach ideal for materials screening.

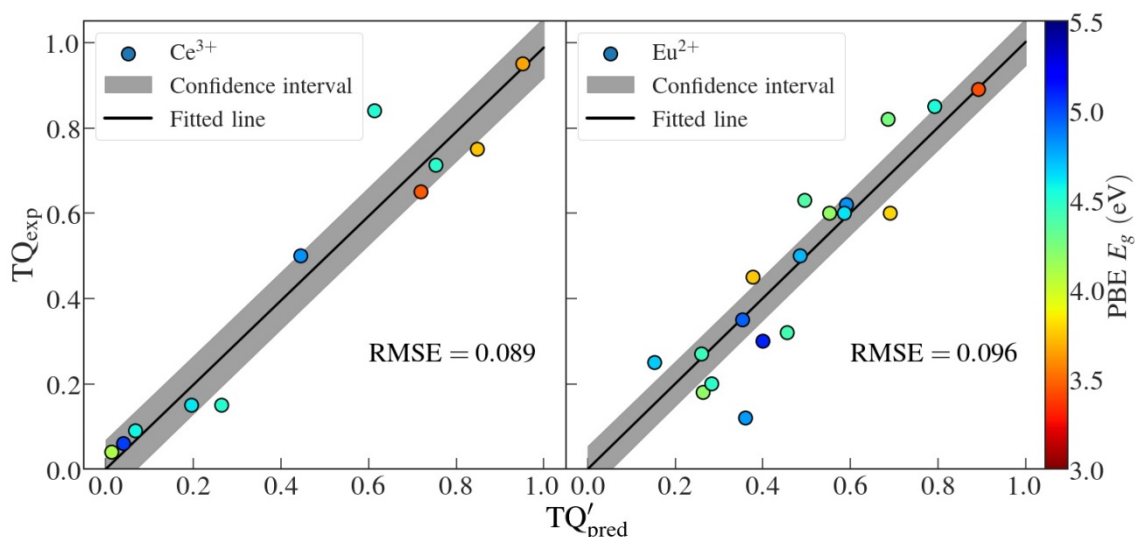


Figure 8. Plot of the predicted TQ_{exp} against TQ'_{pred} obtained from the modified TQ model utilizing the topological descriptor in equation 4 for Ce^{3+} (left) and Eu^{2+} (right)-activated phosphors.

CONCLUSION

In summary, we have developed a unified dual-barrier TQ model by integrating the two prevailing theories – the cross-over and thermal ionization models – for thermal quenching in Ce^{3+} and Eu^{2+} -activated phosphors. More critically, we have developed computational approaches to probe thermal quenching in phosphors using this unified TQ model. We establish that local activator environment stability, as measured by the change in activator environment distribution with temperature in AIMD simulations, ΔAED , is the relevant descriptor for TQ under the cross-over mechanism. The computed host band gap (E_g), the centroid shift (ϵ_c), and the approximated crystal field splitting (ϵ_{cfs}) are descriptors for TQ under the thermal ionization mechanism. This unified dual-barrier thermal quenching model combining ΔAED , E_g , ϵ_c and ϵ_{cfs} predicts the experimentally observed TQ in 29 Ce^{3+} and Eu^{2+} -activated phosphors to within an RMSE of 3.1% and 7.6%, respectively. We have also developed an alternative topological descriptor for local environment stability based on Voronoi tessellation that allows for rapid TQ screening of phosphors without expensive AIMD simulations. This work provides crucial insights into the TQ mechanisms in phosphors, and an efficient and reliable way to the discovery of new phosphors with low TQ for next-generation, high power solid-state lighting.

ASSOCIATED CONTENT

Supporting Information

The Supporting Information is available free of charge on the ACS Publications website at DOI: XXX

Derivation of the Unified Dual-barrier Thermal Quenching model, structural and thermal quenching properties of the 29 oxide phosphors, the activator ($\text{Eu}^{2+}/\text{Ce}^{3+}$) environment distribution in all 29 oxide phosphors, and the Voronoi grid representation of the activator's local environment in the 29 oxide phosphors (PDF)

AUTHOR INFORMATION

Corresponding Author

Shyue Ping Ong – Department of NanoEngineering, University of California, San Diego, La Jolla, California 92093-0448, United States; orcid.org/0000-0001-5726-2587; Phone: (858) 534-2668; Email: ongsp@eng.ucsd.edu

Author Contributions

[†]These authors contributed equally.

Notes

These authors declare no competing financial interest.

ACKNOWLEDGMENT

This work was primarily supported by the National Science Foundation, Ceramics Program, under grant no. 1911372. S. Hariyani and J. Brogch also acknowledge funding from the National Science Foundation under grant no. 1911311 as well as the Division of Materials

Research under grant no. 1847701. The computational resources were provided by the Extreme Science and Engineering Discovering Environment (XSEDE) supported by the National Science Foundation under grant no. ACI-1548562, the Triton Super Computer Center (TSCC) at the University of California, San Diego, and the National Energy Research Scientific Computing Center (NERSC).

REFERENCES

- (1) United Nations Environment Programme. *Accelerating the Global Adoption of Energy-Efficient Lighting - UAE Policy Guide Series*; 2017; Vol. 132.
- (2) Brinkley, S. E.; Pfaff, N.; Denault, K. A.; Zhang, Z.; (Bert) Hintzen, H. T.; Seshadri, R.; Nakamura, S.; DenBaars, S. P. Robust Thermal Performance of $\text{Sr}_2\text{Si}_3\text{N}_8:\text{Eu}^{2+}$: An Efficient Red Emitting Phosphor for Light Emitting Diode Based White Lighting. *Appl. Phys. Lett.* **2011**, *99* (24), 241106. <https://doi.org/10.1063/1.3666785>.
- (3) Poncè, S.; Jia, Y.; Giantomassi, M.; Mikami, M.; Gonze, X. Understanding Thermal Quenching of Photoluminescence in Oxynitride Phosphors from First Principles. *Journal of Physical Chemistry C* **2016**, *120* (7), 4040–4047. <https://doi.org/10.1021/acs.jpcc.5b12361>.
- (4) Denault, K. A.; Brgoch, J.; Kloß, S. D.; Gaultois, M. W.; Siewenie, J.; Page, K.; Seshadri, R. Average and Local Structure, Debye Temperature, and Structural Rigidity in Some Oxide Compounds Related to Phosphor Hosts. *ACS Appl. Mater. Interfaces* **2015**, *7* (13), 7264–7272. <https://doi.org/10.1021/acsami.5b00445>.
- (5) Zhuo, Y.; Mansouri Tehrani, A.; Oliynyk, A. O.; Duke, A. C.; Brgoch, J. Identifying an Efficient, Thermally Robust Inorganic Phosphor Host via Machine Learning. *Nature Communications* **2018**, *9* (1). <https://doi.org/10.1038/s41467-018-06625-z>.
- (6) Dorenbos, P. Thermal Quenching of Eu^{2+} 5d–4f Luminescence in Inorganic Compounds. *Journal of Physics: Condensed Matter* **2005**, *17* (50), 8103–8111. <https://doi.org/10.1088/0953-8984/17/50/027>.
- (7) Blasse, G.; Brill, A. Characteristic Luminescence. *Phil. Tech. Rev.* **1970**, *31* (10), 304–314.
- (8) Blasse, G.; Grabmaier, B. C. *Luminescent Materials*; Springer Berlin Heidelberg: Berlin, Heidelberg, 1994. <https://doi.org/10.1007/978-3-642-79017-1>.
- (9) Ha, J.; Wang, Z.; Novitskaya, E.; Hirata, G. A.; Graeve, O. A.; Ong, S. P.; McKittrick, J. An Integrated First Principles and Experimental Investigation of the Relationship between Structural Rigidity and Quantum Efficiency in Phosphors for Solid State Lighting. *Journal of Luminescence* **2016**, *179*, 297–305. <https://doi.org/10.1016/j.jlumin.2016.07.006>.
- (10) Duke, A. C.; Finley, E.; Hermus, M.; Brgoch, J. Yellow-Green Luminescence and Extreme Thermal Quenching in the $\text{Sr}_6\text{M}_2\text{Al}_4\text{O}_{15}:\text{Eu}^{2+}$ ($\text{M} = \text{Y, Lu, Sc}$) Phosphor Series. *Solid State Sciences* **2016**, *60*, 108–113. <https://doi.org/10.1016/j.solidstatesciences.2016.08.013>.
- (11) Wang, Z.; Chu, I.-H.; Zhou, F.; Ong, S. P. Electronic Structure Descriptor for the Discovery of Narrow-Band Red-Emitting Phosphors. *Chemistry of Materials* **2016**, *28* (11), 4024–4031. <https://doi.org/10.1021/acs.chemmater.6b01496>.
- (12) Kresse, G.; Furthmüller, J. Efficient Iterative Schemes for Ab Initio Total-Energy Calculations Using a Plane-Wave Basis Set. *Physical Review B* **1996**, *54* (16), 11169–11186. <https://doi.org/10.1103/PhysRevB.54.11169>.
- (13) Blöchl, P. E. Projector Augmented-Wave Method. *Phys. Rev. B* **1994**, *50* (24), 17953–17979. <https://doi.org/10.1103/PhysRevB.50.17953>.
- (14) Perdew, J. P.; Burke, K.; Ernzerhof, M. Generalized Gradient Approximation Made Simple. *Physical Review Letters* **1996**, *77* (18), 3865–3868. <https://doi.org/10.1103/PhysRevLett.77.3865>.
- (15) Ong, S. P.; Cholia, S.; Jain, A.; Brafman, M.; Gunter, D.; Ceder, G.; Persson, K. A. The Materials Application Programming Interface (API): A Simple, Flexible and Efficient API for Materials Data Based on REpresentational State Transfer (REST) Principles. *Computational Materials Science* **2015**, *97*, 209–215. <https://doi.org/10.1016/j.commatsci.2014.10.037>.
- (16) Chaudhry, A.; Boutchko, R.; Chourou, S.; Zhang, G.; Grønbech-Jensen, N.; Canning, A. First-Principles Study of Luminescence in Eu^{2+} -Doped Inorganic Scintillators. *Phys. Rev. B* **2014**, *89* (15), 155105. <https://doi.org/10.1103/PhysRevB.89.155105>.
- (17) Ong, S. P.; Richards, W. D.; Jain, A.; Hautier, G.; Kocher, M.; Cholia, S.; Gunter, D.; Chevrier, V. L.; Persson, K. A.; Ceder, G. Python Materials Genomics (Pymatgen): A Robust, Open-Source Python Library for Materials Analysis. *Computational Materials Science* **2013**, *68*, 314–319. <https://doi.org/10.1016/j.commatsci.2012.10.028>.
- (18) Hoover, W. G. Hoover WG (1985) Canonical Dynamics: Equilibrium Phase-Space Distributions. *Phys Rev A* **31**:1695–1697 . Doi: 10.1103/PhysRevA.31.1695. **1985**, *31* (3), 1695–1697.
- (19) Brgoch, J.; DenBaars, S. P.; Seshadri, R. Proxies from Ab Initio Calculations for Screening Efficient Ce^{3+} Phosphor Hosts. *The Journal of Physical Chemistry C* **2013**, *117* (35), 17955–17959. <https://doi.org/10.1021/jp405858e>.
- (20) Waroquiers, D.; Gonze, X.; Rignanese, G. M.; Welker-Nieuwoudt, C.; Rosowski, F.; Göbel, M.; Schenk, S.; Degelmann, P.; André, R.; Glaum, R.; Hautier, G. Statistical Analysis of Coordination Environments in Oxides. *Chemistry of Materials* **2017**, *29* (19), 8346–8360. <https://doi.org/10.1021/acs.chemmater.7b02766>.
- (21) Hoppe, R. The Coordination Number. **1970**, *9* (I), 25–34.
- (22) Dorenbos, P. A Review on How Lanthanide Impurity Levels Change with Chemistry and Structure of Inorganic Compounds. *ECSSJ. Solid State Sci. Technol.* **2013**, *2* (2), R3001–R3011. <https://doi.org/10.1149/2.001302jss>.
- (23) Dorenbos, P. Ce^{3+} 5d-Centroid Shift and Vacuum Referred 4f-Electron Binding Energies of All Lanthanide Impurities in 150 Different Compounds. *Journal of Luminescence* **2013**, *135*, 93–104. <https://doi.org/10.1016/j.jlumin.2012.09.034>.
- (24) Dorenbos, P. Relating the Energy of the [Xe] 5d 1 Configuration of Ce^{3+} in Inorganic Compounds with Anion Polarizability and Cation Electronegativity. *Phys. Rev. B* **2002**, *65* (23), 235110. <https://doi.org/10.1103/PhysRevB.65.235110>.
- (25) Görrler-Walrand, C.; Binnemans, K. Chapter 155 Rationalization of Crystal-Field Parametrization. In *Handbook on the Physics and Chemistry of Rare Earths*; Elsevier, 1996; Vol. 23, pp 121–283. [https://doi.org/10.1016/S0168-1273\(96\)23006-5](https://doi.org/10.1016/S0168-1273(96)23006-5).
- (26) Dorenbos, P. 5d – Level Energies of Ce^{3+} and the Crystalline Environment. II. Chloride, Bromide, and Iodide Compounds. *Phys. Rev. B* **2000**, *62* (23), 15650–15659. <https://doi.org/10.1103/PhysRevB.62.15650>.
- (27) Nemitz, W.; Fulmek, P.; Nicolics, J.; Reil, F.; Wenzl, F. P. On the Determination of the Temperature Distribution within the Color Conversion Elements of Phosphor Converted LEDs. *Sci Rep* **2017**, *7*. <https://doi.org/10.1038/s41598-017-10114-6>.
- (28) Ueda, J.; Dorenbos, P.; Bos, A. J. J.; Meijerink, A.; Tanabe, S. Insight into the Thermal Quenching Mechanism for $\text{Y}_3\text{Al}_5\text{O}_{12}:\text{Ce}^{3+}$ through Thermoluminescence Excitation Spectroscopy. *The Journal of Physical Chemistry C* **2015**, *119* (44), 25003–25008. <https://doi.org/10.1021/acs.jpcc.5b08828>.
- (29) Nien, Y. T.; You, J. K. Improved Thermal Quenching of $\text{Y}_3\text{Al}_5\text{O}_{12}:\text{Ce}$ Phosphor Ceramics with Silica Addition. *Journal of Alloys and Compounds* **2016**, *678*, 1–4. <https://doi.org/10.1016/j.jallcom.2016.03.297>.
- (30) Brgoch, J.; Hasz, K.; Denault, K. A.; Borg, C. K. H.; Mikhailovsky, A. A.; Seshadri, R. Data-Driven Discovery of Energy Materials: Efficient $\text{BaM}_2\text{Si}_3\text{O}_{10}:\text{Eu}^{2+}$ ($\text{M} = \text{Sc, Lu}$) Phosphors for Application in Solid State White Lighting. *Faraday Discussions* **2014**, *176*, 333–347. <https://doi.org/10.1039/c4fd00125g>.
- (31) Hermus, M.; Phan, P.-C.; Brgoch, J. Ab Initio Structure Determination and Photoluminescent Properties of an Efficient, Thermally Stable Blue Phosphor, $\text{Ba}_2\text{Y}_5\text{B}_3\text{O}_{17}:\text{Ce}^{3+}$. *Chem. Mater.* **2016**, *28* (4), 1121–1127. <https://doi.org/10.1021/acs.chemmater.5b04542>.
- (32) Wang, Z.; Ha, J.; Kim, Y. H.; Im, W. B.; McKittrick, J.; Ong, S. P. Mining Unexplored Chemistries for Phosphors for High-Color-Quality White-Light-Emitting Diodes. *Joule* **2018**, *2* (5), 914–926. <https://doi.org/10.1016/j.joule.2018.01.015>.
- (33) ZHOU, W.; MA, X.; ZHANG, M.; LUO, Y.; XIA, Z. Effect of Different RE Dopants on Phosphorescence Properties of $\text{Sr}_2\text{Al}_2\text{SiO}_7:\text{Eu}^{2+}$ Phosphors. *Journal of Rare Earths* **2015**, *33* (7), 700–705. [https://doi.org/10.1016/S1002-0721\(14\)60473-7](https://doi.org/10.1016/S1002-0721(14)60473-7).

- (34) Lu, F.-C.; Bai, L.-J.; Dang, W.; Yang, Z.-P.; Lin, P. Structure and Photoluminescence of Eu²⁺ Doped Sr₂Al₂SiO₇ Cyan-Green Emitting Phosphors. *ECS Journal of Solid State Science and Technology* **2014**, *4* (2), R27–R30. <https://doi.org/10.1149/2.0151502jss>.
- (35) Li, Y. Q.; Hirosaki, N.; Xie, R. J.; Mitomo, M. Crystal, Electronic and Luminescence Properties of Eu²⁺-Doped Sr₂Al_{2-x}Si_{1+x}O_{7-x}N_x. *Science and Technology of Advanced Materials* **2007**, *8* (7–8), 607–616. <https://doi.org/10.1016/j.stam.2007.08.007>.
- (36) Komuro, N.; Mikami, M.; Shimomura, Y.; Bithell, E. G.; Cheetham, A. K. Synthesis, Structure and Optical Properties of Europium Doped Calcium Barium Phosphate – a Novel Phosphor for Solid-State Lighting. *Journal of Materials Chemistry C* **2014**, *2* (30), 6084–6084. <https://doi.org/10.1039/C4TC00732H>.
- (37) Dorenbos, P. Relation between Eu²⁺ and Ce³⁺ f d-Transition Energies in Inorganic Compounds. *J. Phys.: Condens. Matter* **2003**, *15* (27), 4797–4807. <https://doi.org/10.1088/0953-8984/15/27/311>.
- (38) Perdew, J. P. Density Functional Theory and the Band Gap Problem. *Int. J. Quantum Chem.* **2009**, *28* (S19), 497–523. <https://doi.org/10.1002/qua.560280846>.
- (39) Hölsä, J.; Kirm, M.; Laamanen, T.; Lastusaari, M.; Niittykoski, J.; Novák, P. Electronic Structure of the Sr₂MgSi₂O₇:Eu²⁺ Persistent Luminescence Material. *Journal of Luminescence* **2009**, *129* (12), 1560–1563. <https://doi.org/10.1016/j.jlumin.2009.04.042>.
- (40) Müller, M.; Volhard, M. F.; Jüstel, T. Photoluminescence and Afterglow of Deep Red Emitting SrSc₂O₄:Eu²⁺. *RSC Advances* **2016**, *6* (10), 8483–8488. <https://doi.org/10.1039/c5ra25686k>.
- (41) Qiao, J.; Amachraa, M.; Molokeev, M.; Chuang, Y.-C.; Ong, S. P.; Zhang, Q.; Xia, Z. Engineering of K₃YSi₂O₇ To Tune Photoluminescence with Selected Activators and Site Occupancy. *Chem. Mater.* **2019**. <https://doi.org/10.1021/acs.chemmater.9b02990>.
- (42) Kim, Y. H.; Arunkumar, P.; Kim, B. Y.; Unithrattil, S.; Kim, E.; Moon, S.-H.; Hyun, J. Y.; Kim, K. H.; Lee, D.; Lee, J.-S.; Im, W. B. A Zero-Thermal-Quenching Phosphor. *Nature Materials* **2017**, *16* (5), 543–550. <https://doi.org/10.1038/nmat4843>.
- (43) Pinsky, M.; Avnir, D. Continuous Symmetry Measures. 5. The Classical Polyhedra. *Inorganic Chemistry* **1998**, *37* (21), 5575–5582. <https://doi.org/10.1021/ic9804925>.
- (44) Duke, A. C.; Hariyani, S.; Brgoch, J. Ba₃Y₂B₆O₁₅:Ce³⁺ —A High Symmetry, Narrow-Emitting Blue Phosphor for Wide-Gamut White Lighting. *Chem. Mater.* **2018**, *30* (8), 2668–2675. <https://doi.org/10.1021/acs.chemmater.8b00111>.

Supporting Information

Unified Theory of Thermal Quenching in Inorganic Phosphors

Mahdi Amachraa^{a†}, Zhenbin Wang^{b†}, Chi Chen^b, Shruti Hariyani^c, Hanmei Tang^a, Jakoah Brgoch^c, Shyue Ping Ong^{b*}

^aMaterials Science and Engineering Program, University of California San Diego, 9500 Gilman Dr, Mail Code 0418, La Jolla, CA 92093-0448, United States

^bDepartment of NanoEngineering, University of California San Diego, 9500 Gilman Dr, Mail Code 0448, La Jolla, CA 92093-0448, United States

^cDepartment of Chemistry, University of Houston, College of Natural Sciences and Mathematics, Science & Research Building 1, 3507 Cullen Blvd, Room 214, Houston, Texas 77204-5008

Corresponding Author

* ongsp@eng.ucsd.edu (S. P. Ong)

Derivation of Unified Thermal Quenching Model

The quantum efficiency (QE) of electronic transitions¹ is given by:

$$\text{QE}(T) = \frac{1}{1 + \Gamma e^{\frac{-E_a}{k_B T}}}$$

$$\Gamma = \frac{\Gamma_0}{\Gamma_v}$$

where the constant Γ is defined as the ratio of the attempt rate for thermal quenching (Γ_0) and the radiative decay rate of the $5d$ state (Γ_v), k_B is Boltzmann's constant, and E_a is the activation energy for the mechanism of loss of emission. The constant C for Eu^{2+} and Ce^{3+} have previously been derived by Dorenbos as 2.37×10^7 and as 2.3×10^6 respectively.^{2,3}

The thermal stability (TS) of a phosphor compound is measured as the ratio of the QE between a lower temperature T_1 and a higher temperature T_2 , as follows:

$$\text{TS} = \frac{\text{QE}(T_2)}{\text{QE}(T_1)} = \frac{1 + \Gamma e^{\frac{-E_a}{k_B T_1}}}{1 + \Gamma e^{\frac{-E_a}{k_B T_2}}}$$

Throughout this work, $T_1 = 300$ K and $T_2 = 500$ K. The thermal quenching rate is simply given by:

$$\text{TQ} = 1 - \text{TS}$$

Assuming that the cross-over and thermal ionization mechanisms operate independently, the overall TS is then given by:

$$\text{TS} = \text{TS}^{co} \text{TS}^i = (1 - K\Delta\text{AED}) \frac{1 + \Gamma e^{\frac{-E_a}{k_B T_1}}}{1 + \Gamma e^{\frac{-E_a}{k_B T_2}}}$$

where ΔAED is the change in local activator environment distribution, the assumption that TS^{co} is a linear function of ΔAED is used and K is a fitted constant, and E_a being the activation energy barrier under the Dorenbos thermal ionization model can be denoted as E_a^i . Therefore, the overall TQ model is given as:

$$\text{TQ} = 1 - \text{TS}^{co} \text{TS}^i = 1 - (1 - K\Delta\text{AED}) \frac{1 + \Gamma e^{\frac{-E_a^i}{k_B T_1}}}{1 + \Gamma e^{\frac{-E_a^i}{k_B T_2}}} \quad (\text{S1})$$

where, a thorough derivation of E_a^i is elaborated and included the Main manuscript as follows:

$$E_a^i = AE_g^{DFT} + B\epsilon_c^{DFT} + \frac{1}{r} \left(C \frac{\theta_0^2}{l_{avg}^3} + D \frac{\theta_0^4}{l_{avg}^5} \right) + E \quad (\text{S2})$$

l_{avg} refers to the average bond length as defined in equation 1 in the Main manuscript. Finally, using equation S2 and the results from the AIMD simulations (ΔAED), equation S1 can be solved by fitting the unknown constants K , A , B , C , D and E . The constants were determined by performing a least-square minimization of the predicted TQ from equation S1 with the experimentally-observed TQ of the 29 phosphors (given in Table S1). This minimization was carried out using the SciPy package using the BFGS algorithm.⁷ All of the computed ϵ_c^{DFT} are tabulated in Table S1.

Table S1. Structural and thermal quenching properties for 29 oxide phosphors. The TQ data presented here is experimental value collected from corresponding cited references. Act stands for activator. G:CN is the activator's local environment (C=cube, O=octahedron, TP=trigonal prism, 1CTP=mono-capped trigonal prism, 2CTP=bi-capped trigonal prism, I=icosahedron) E_g (unit: eV) is the host band gap calculated using the PBE functional. ϵ_c (unit: eV) is the computed centroid shift. ΔAED is the difference in the activator environment distribution (AED) between 300 K and 500 K. The computed Voronoi area is denoted by $Area(Y)$. E_a^i (unit: eV) is the predicted activation energy. Θ_D (unit: K) is DFT calculated Debye temperature using PBE functional.

Host material	Space group	Act	G:CN	TQ%	E_g	ϵ_c^{DFT}	ΔAED	Area(Y)%	E_a^i	Θ_D	Refs.
Lu ₃ Al ₅ O ₁₂	$Ia\bar{3}d$	Ce ³⁺	C:8	6	5.04	1.78	0.032	88.2	0.86	605.8	3,8,9
Ba ₉ Lu ₂ Si ₆ O ₂₄	$R\bar{3}$	Ce ³⁺	O:6	15	4.62	1.86	0.029	86.6	0.74	398.3	10
Y ₃ Al ₅ O ₁₂	$Ia\bar{3}d$	Ce ³⁺	C:8	9	4.58	2.25	0.027	78.4	0.88	712.8	3,11,12
Ca ₃ Sc ₂ Si ₃ O ₁₂	$Ia\bar{3}d$	Ce ³⁺	C:8	4	4.10	1.75	0.020	80.0	1.00	672.6	13-15
Ba ₉ Y ₂ Si ₆ O ₂₄	$R\bar{3}$	Ce ³⁺	C:8	15	4.51	1.84	0.016	86.0	0.72	388.3	16
BaLu ₂ Si ₃ O ₁₀	$P2_1/m$	Ce ³⁺	O:6	50	4.82	1.38	0.093	14.5	0.71	406.5	17
Ba ₂ Y ₃ B ₅ O ₁₇	$Pbcn$	Ce ³⁺	O:6	71	4.50	1.23	0.120	38.0	0.63	392.4	18
Y ₃ Mg ₂ AlSi ₂ O ₁₂	$Ia\bar{3}d$	Ce ³⁺	C:8	75	3.94	1.68	0.100	12.0	0.61	652.0	19
Gd ₃ Al ₅ O ₁₂	$Ia\bar{3}d$	Ce ³⁺	C:8	65	3.46	1.78	0.080	79.1	0.63	500.9	20
Ba ₃ Y ₂ B ₆ O ₁₅	$Ia\bar{3}$	Ce ³⁺	O:6	84	4.52	1.24	0.180	95.0	0.64	379.0	21
K ₃ YSi ₂ O ₇	$P6_3/mmc$	Ce ³⁺	TP:6	95	3.67	1.46	0.145	95.0	0.54	515.2	22
SrMgAl ₁₀ O ₁₇	$P6_3/mmc$	Eu ²⁺	TP:6	12	4.80	0.63	0.043	50.0	0.93	656.9	23,24
KSrPO ₄	Pm	Eu ²⁺	1CTP:7	30	5.10	0.78	0.120	47.8	1.03	292.8	25,26
KBaPO ₄	Pnm	Eu ²⁺	1CTP:7	35	4.95	0.77	0.127	54.0	1.00	332.9	26,27
Sr ₂ LiAlO ₄	$P2_1/m$	Eu ²⁺	TP:6	12	4.19	1.25	0.028	79.0	0.82	467.5	28
BaZrSi ₃ O ₉	$P\bar{6}2c$	Eu ²⁺	O:6	25	4.68	0.63	0.112	80.0	1.25	493.1	29,30
BaSc ₂ Si ₃ O ₁₀	$P2_1/m$	Eu ²⁺	2CTP:8	50	4.73	0.90	0.172	37.0	0.96	529.2	31
Sr ₃ SiO ₅	$P4/ncc$	Eu ²⁺	2CTP:8	45	3.76	1.53	0.080	82.0	0.78	402.7	32-34
Ba ₂ MgSi ₂ O ₇	$C2/c$	Eu ²⁺	O:6	27	4.45	0.71	0.063	66.0	1.20	386.6	35
SrLiPO ₄	$P6_3$	Eu ²⁺	I:12	32	4.42	0.99	0.118	41.6	0.92	378.9	26
Sr ₂ SiO ₄	$Pmcm$	Eu ²⁺	TP:6	63	4.38	1.09	0.156	38.0	0.88	431.7	36
BaLu ₂ Si ₃ O ₁₀	$P2_1/m$	Eu ²⁺	2CTP:8	62	4.82	0.94	0.213	23.0	0.98	406.5	37
Sr ₂ Al ₂ SiO ₇	$P\bar{4}2_1m$	Eu ²⁺	TP:6	60	4.20	1.08	0.111	37.0	0.75	514.6	38-40
Ba ₂ SiO ₄	$Pmcm$	Eu ²⁺	1CTP:7	60	4.63	1.08	0.216	24.0	0.94	311.3	36
Ca ₆ BaP ₄ O ₁₇	$C2/m$	Eu ²⁺	2CTP:8	82	4.26	1.04	0.189	12.0	0.88	507.8	41
Ca ₇ Mg(SiO ₄) ₄	$Pnm2$	Eu ²⁺	TP:6	60	4.18	1.51	0.108	34.5	0.83	601.0	42
CaMgSi ₂ O ₆	$Pmcm$	Eu ²⁺	C:8	75	4.55	1.18	0.204	25.0	0.73	665.0	42
Sr ₂ MgSi ₂ O ₇	$P\bar{4}2_1m$	Eu ²⁺	TP:6	20	4.49	0.64	0.059	68.0	0.87	475.7	43
SrSc ₂ O ₄	$Pnma$	Eu ²⁺	2CTP:8	89	3.44	1.67	0.160	8.38	0.71	604.7	44

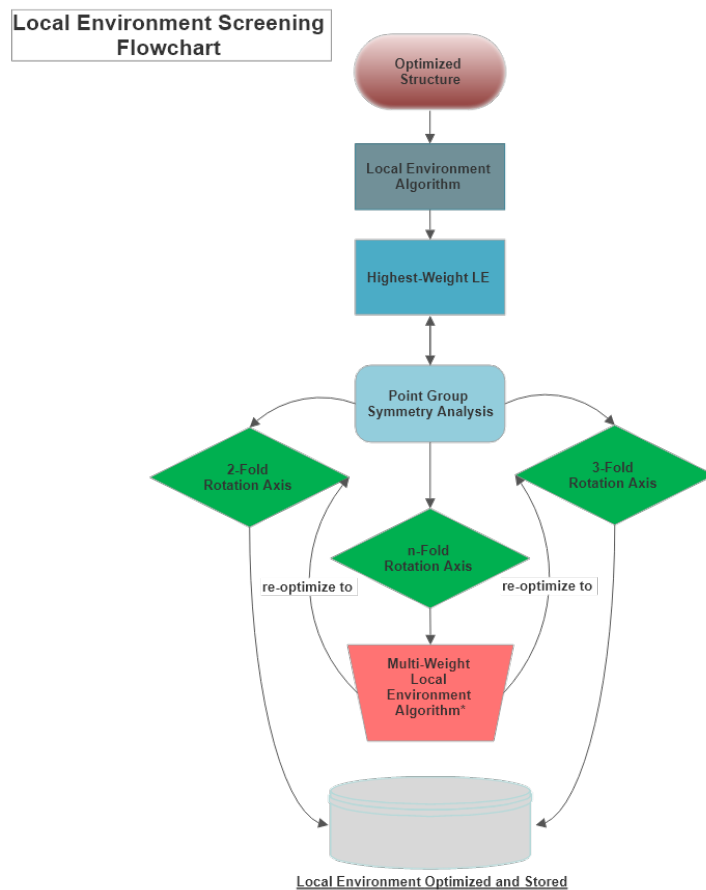


Figure S1. Flowchart showing how the local environment (LE) is determined. The highest-weight local environment is obtained by computing the effective coordination number and effective bond weights as developed by Hoppe. The point group symmetry analysis is conducted by the python materials genomics software (pymatgen). Waroquiers's LE algorithm is utilized to compute a multi-weight interrelation by simulating small atomic displacements. Finally, the highest LE is re-optimized to either have a 3-fold or 2-fold rotation axis.

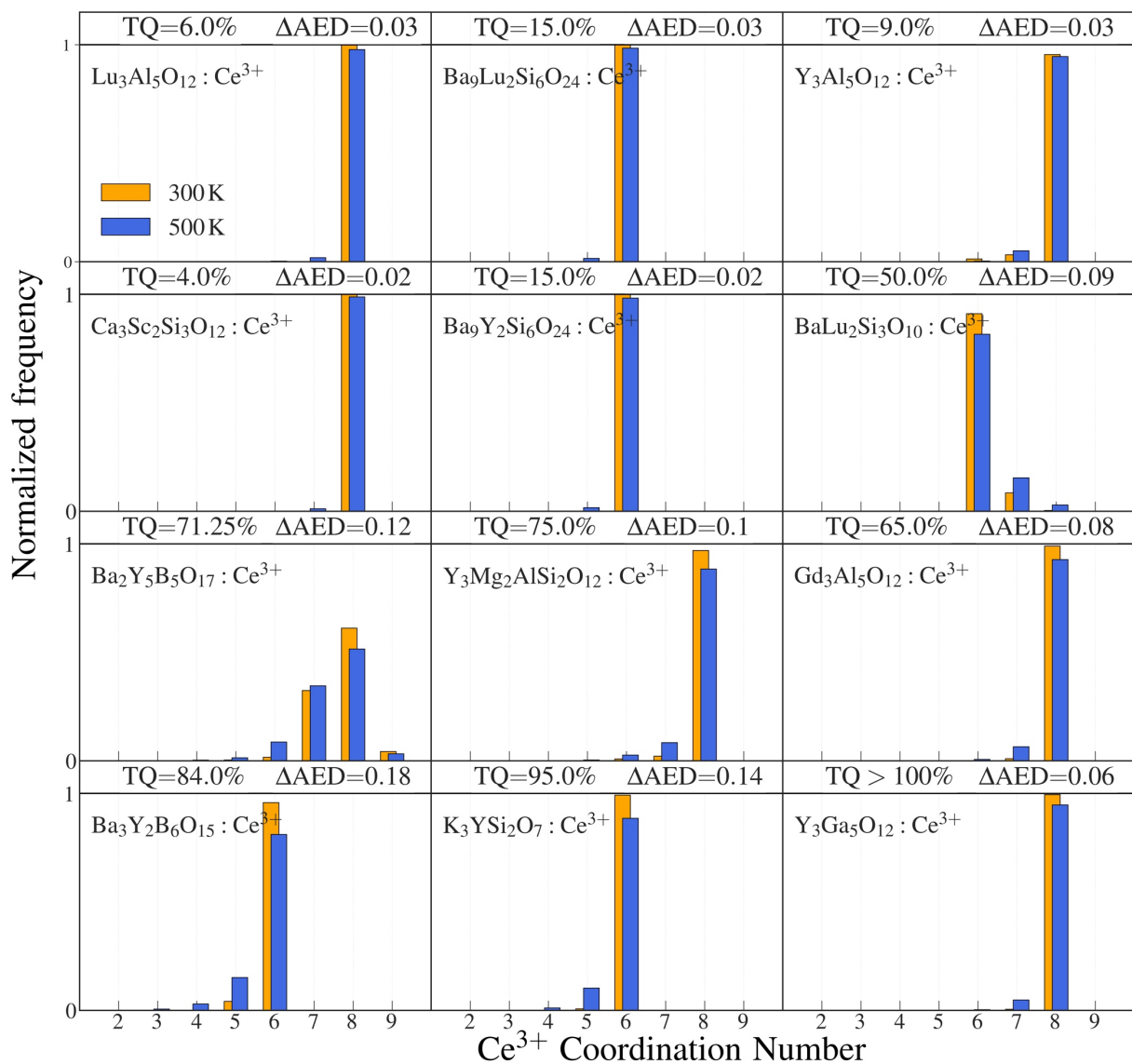


Figure S2. The activator environment distribution for Ce^{3+} -activated hosts at 300 K and 500 K. Experimental TQ rates as well as the computed ΔAED are shown. Note, the TQ rate of $\text{Y}_3\text{Ga}_5\text{O}_{12}:\text{Ce}^{3+}$ is not applicable here, as its quantum efficiency is measured to be 0 between 300 K and 500 K. The AED of $\text{Y}_3\text{Ga}_5\text{O}_{12}:\text{Ce}^{3+}$ are shown for comparison purposes between other garnet structures.

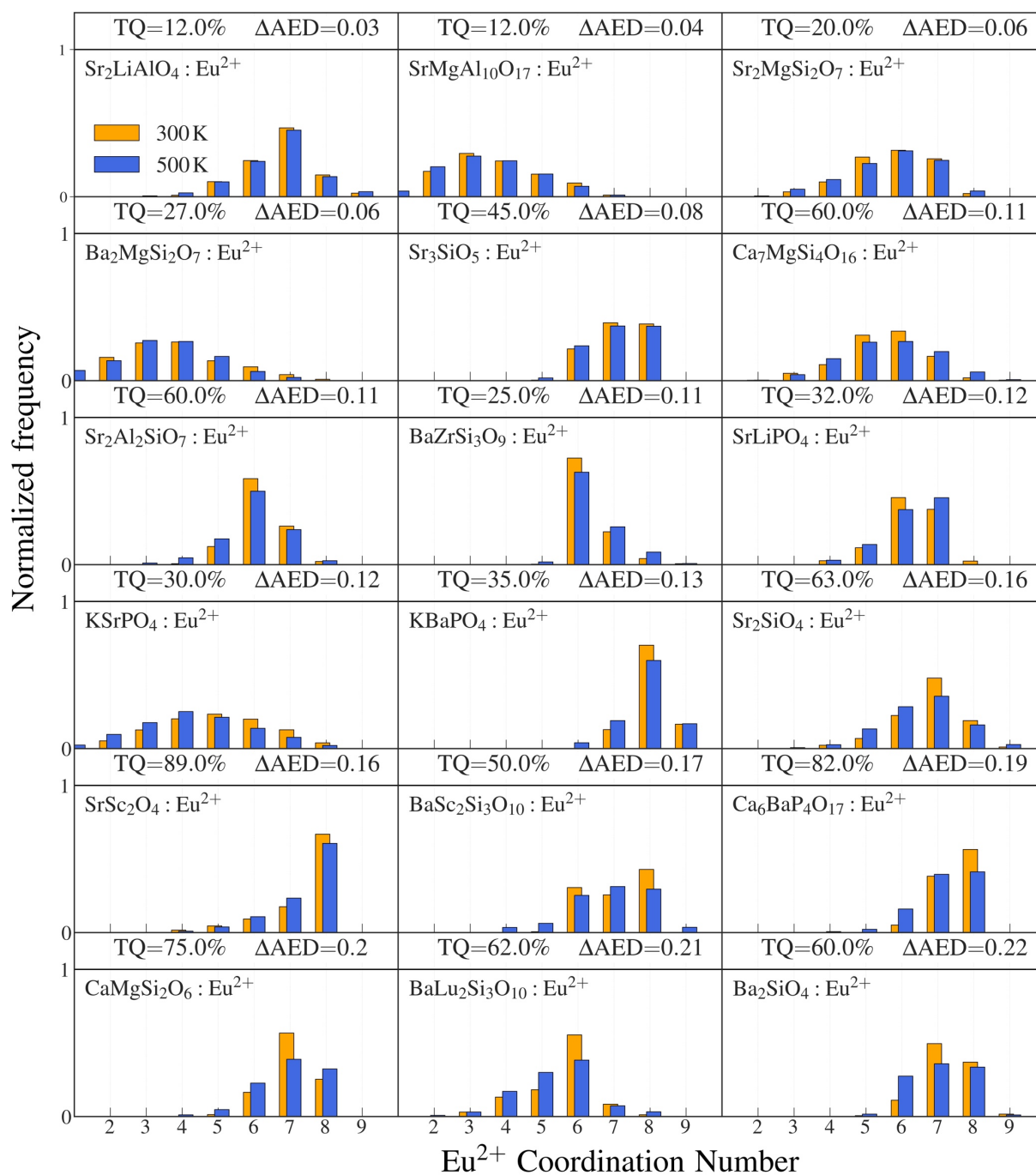


Figure S3. The activator environment distribution for Eu^{2+} -activated hosts at 300 K and 500 K. Experimental TQ rates as well as the computed ΔAED are shown.

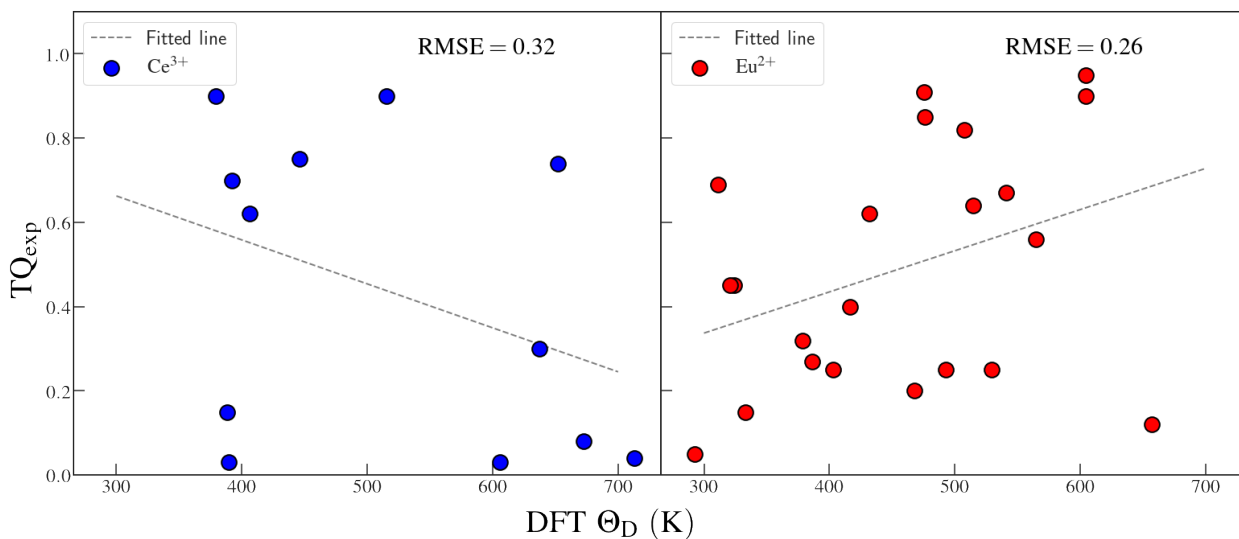


Figure S4. Experimentally measured thermal quenching (TQ_{exp}) against the DFT-calculated Debye temperature (Θ_D).

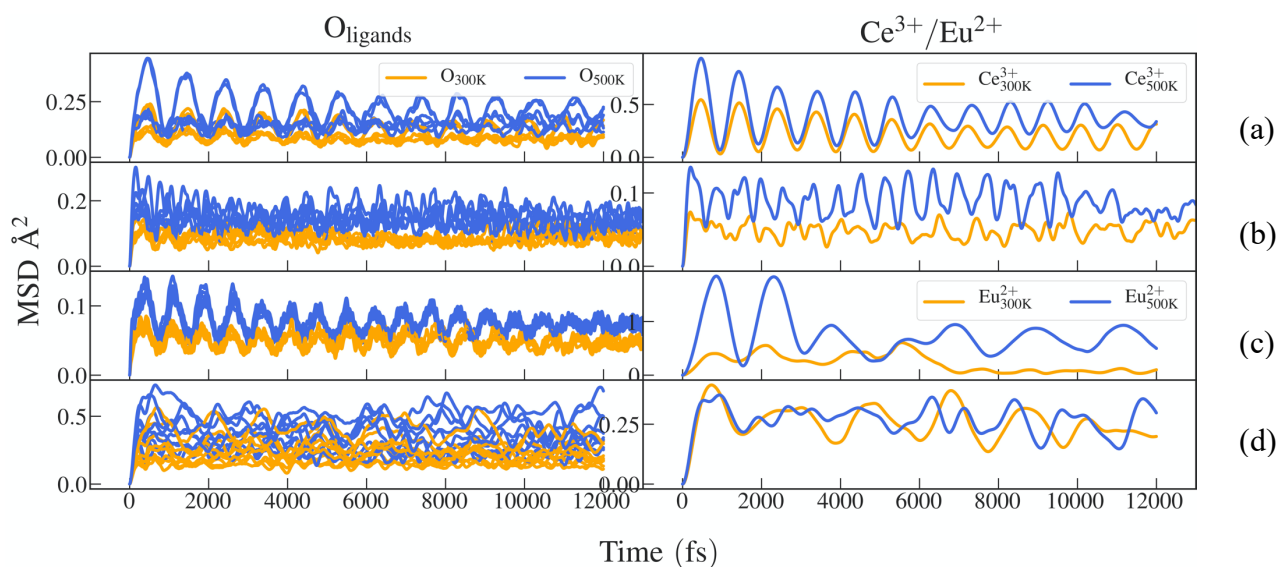
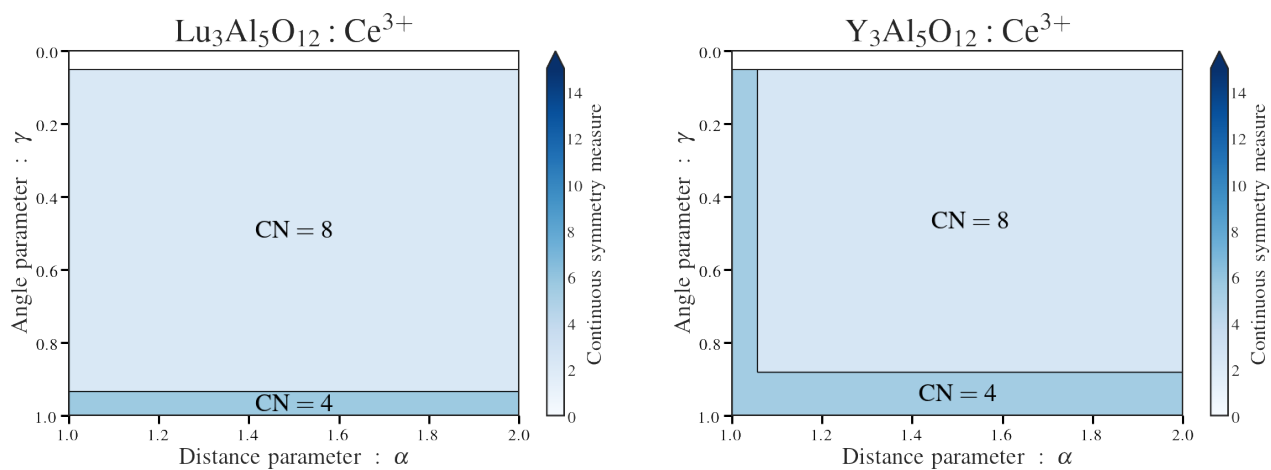
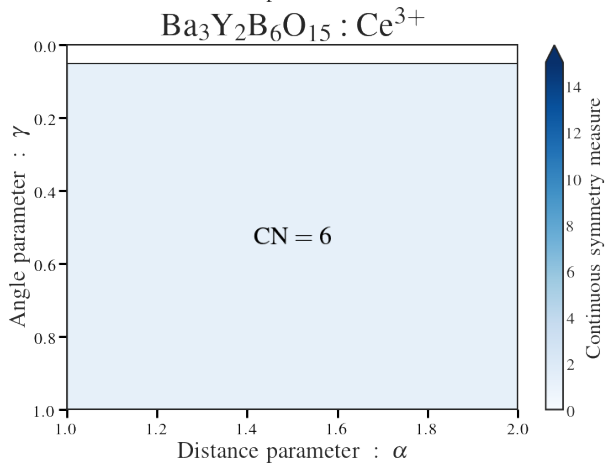
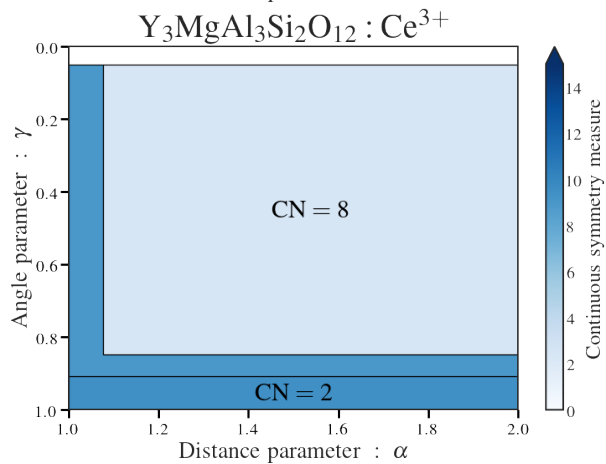
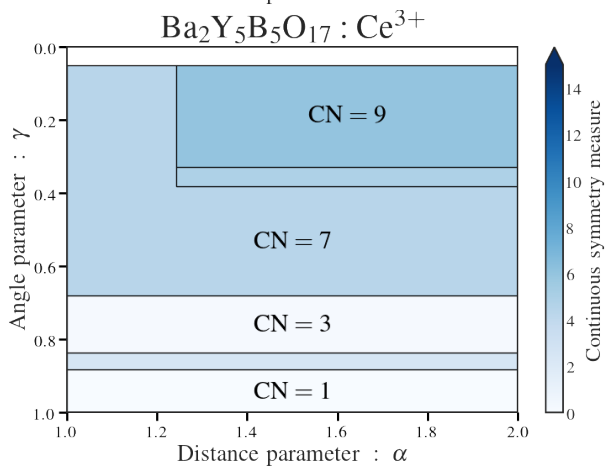
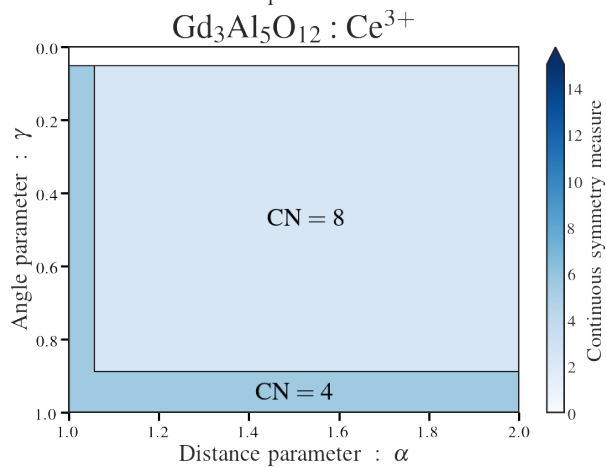
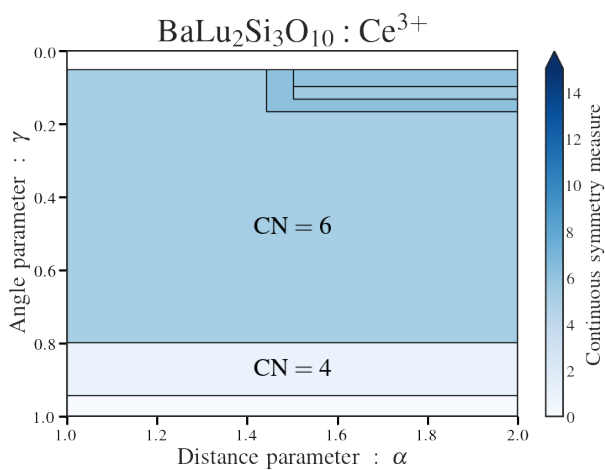
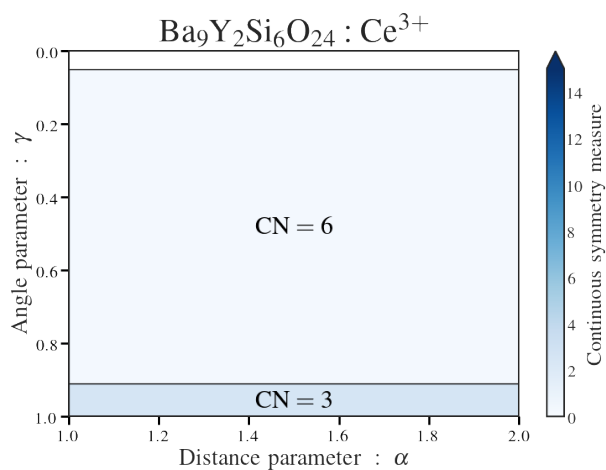
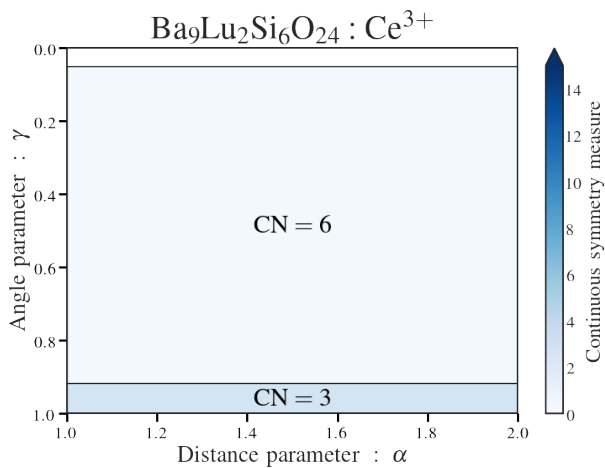
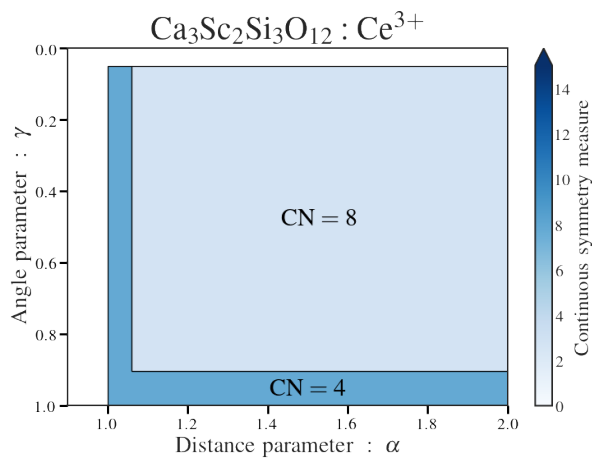


Figure S5. The mean-square displacements (MSD) against time (fs) of $\text{Ce}^{3+}/\text{Eu}^{2+}$ and oxygen ligands ($\text{O}_{\text{ligands}}$) in (a) $\text{Ca}_3\text{Sc}_2\text{Si}_3\text{O}_{12}$, (b) $\text{Ba}_3\text{Y}_2\text{B}_5\text{O}_{15}$, (c) $\text{SrMgAl}_{10}\text{O}_{17}$, and (d) Ba_2SiO_4 host. Note, the left-hand plots refer to the MSD behavior of oxygen ligands in the first shell, while the right-hand plots refer to the MSD behavior of Ce^{3+} and Eu^{2+} activator in the doped supercells.





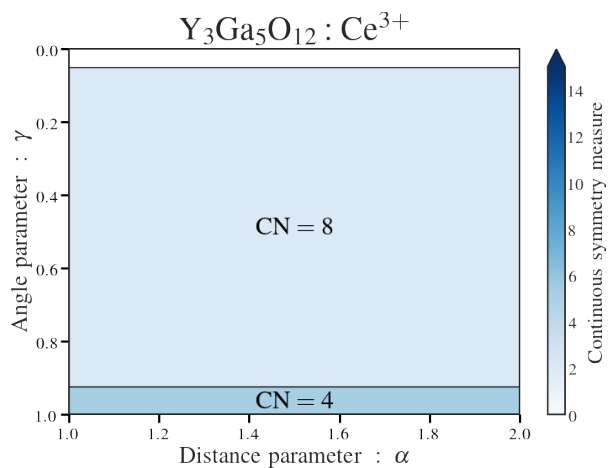
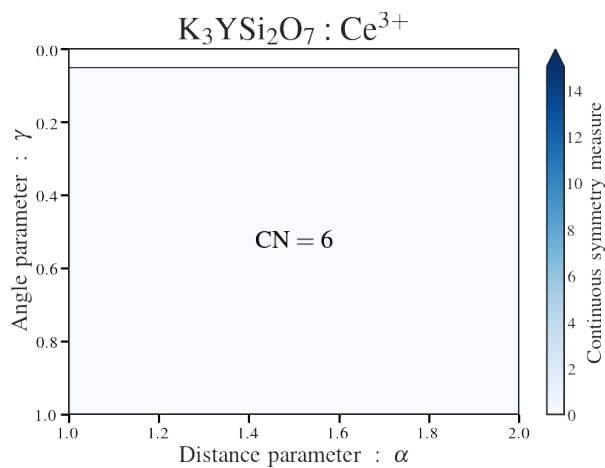
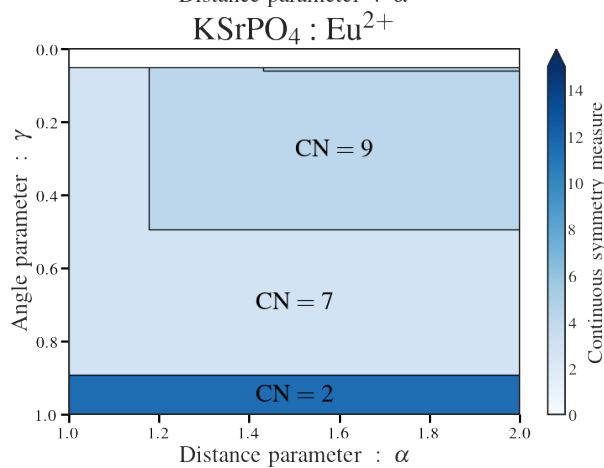
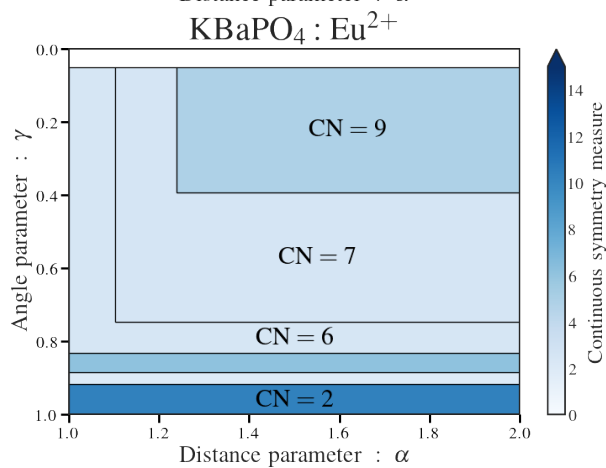
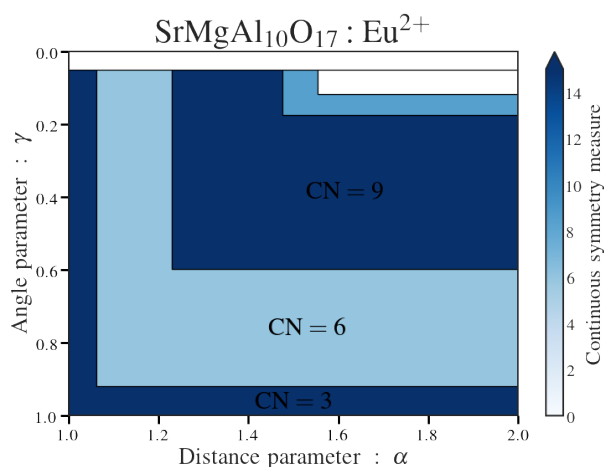
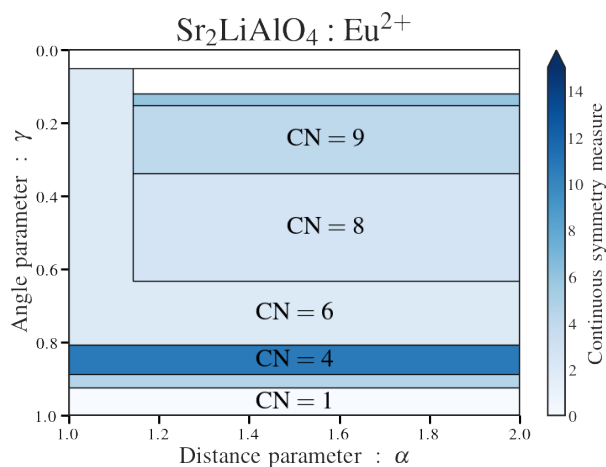
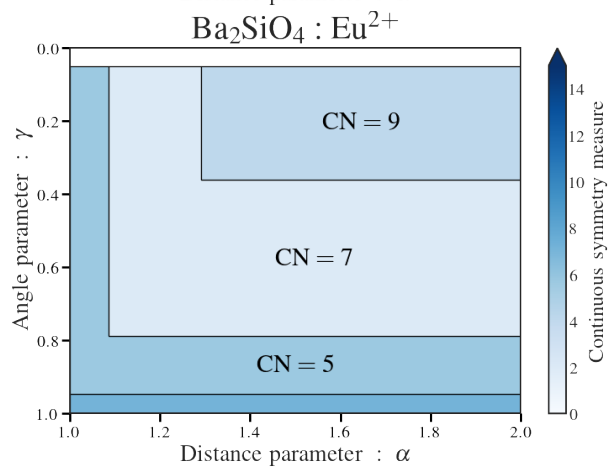
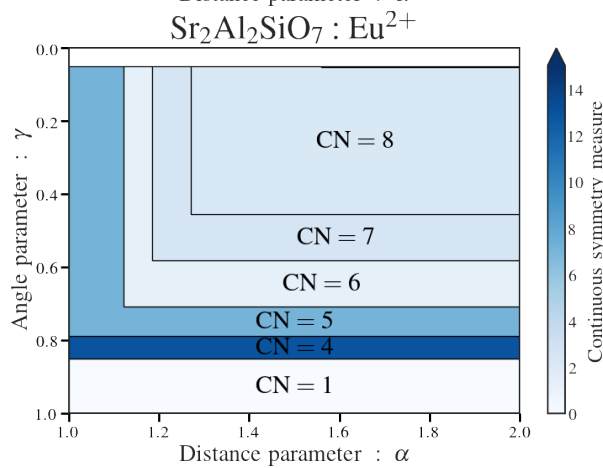
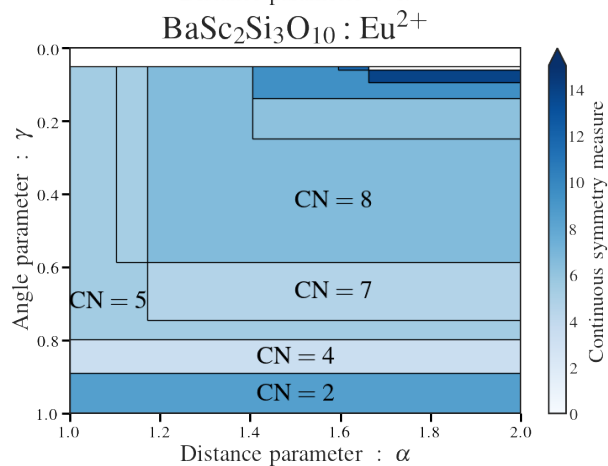
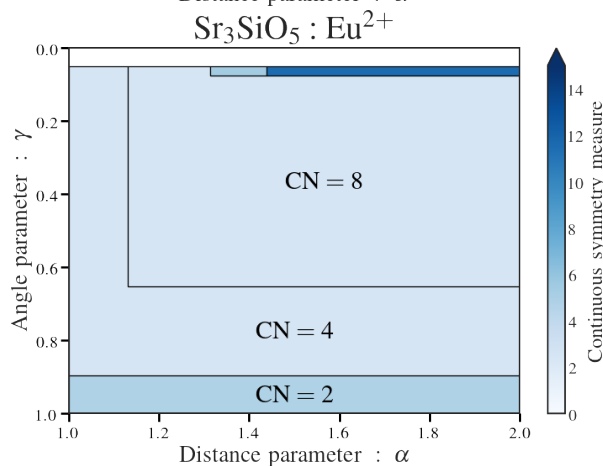
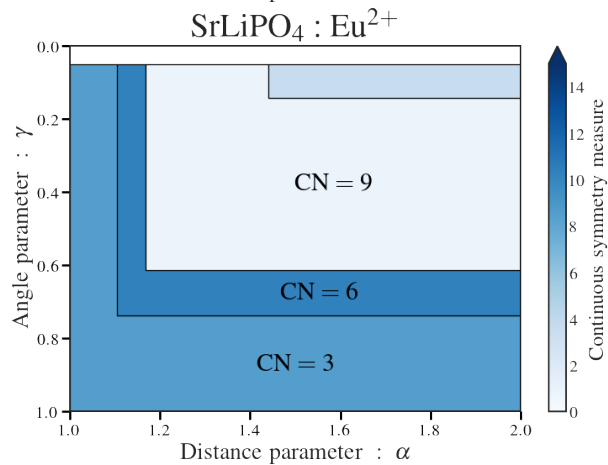
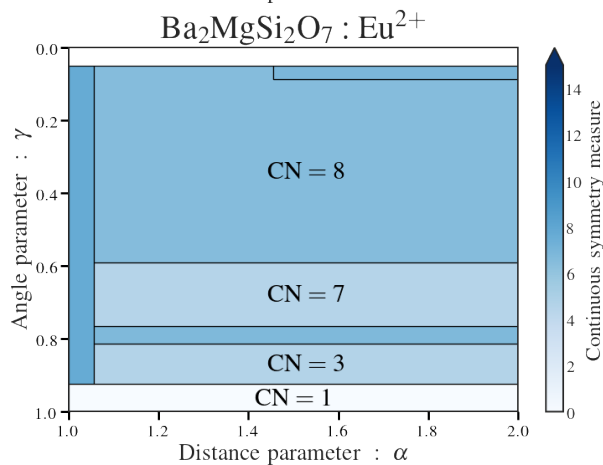
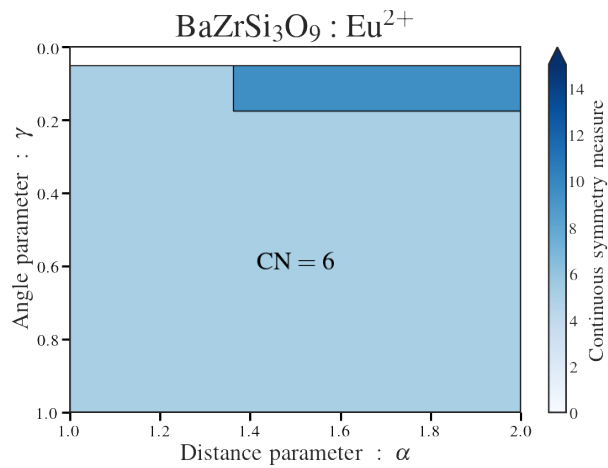
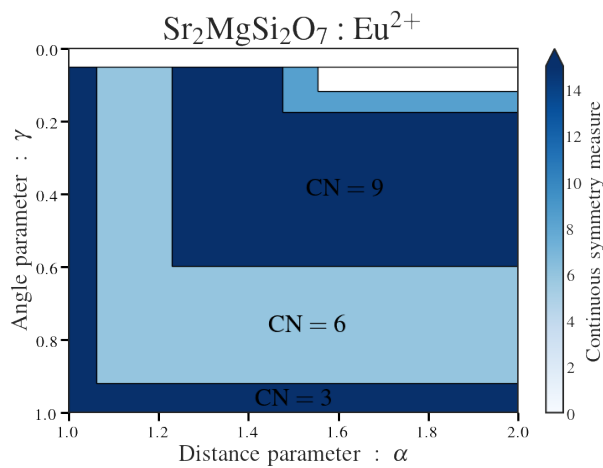


Figure S6. The Voronoi grid representation of Ce^{3+} local environment of all Ce^{3+} -activated hosts in Table S1. The coordination number (CN) in red reflects the environment considered to compute the Voronoi area.





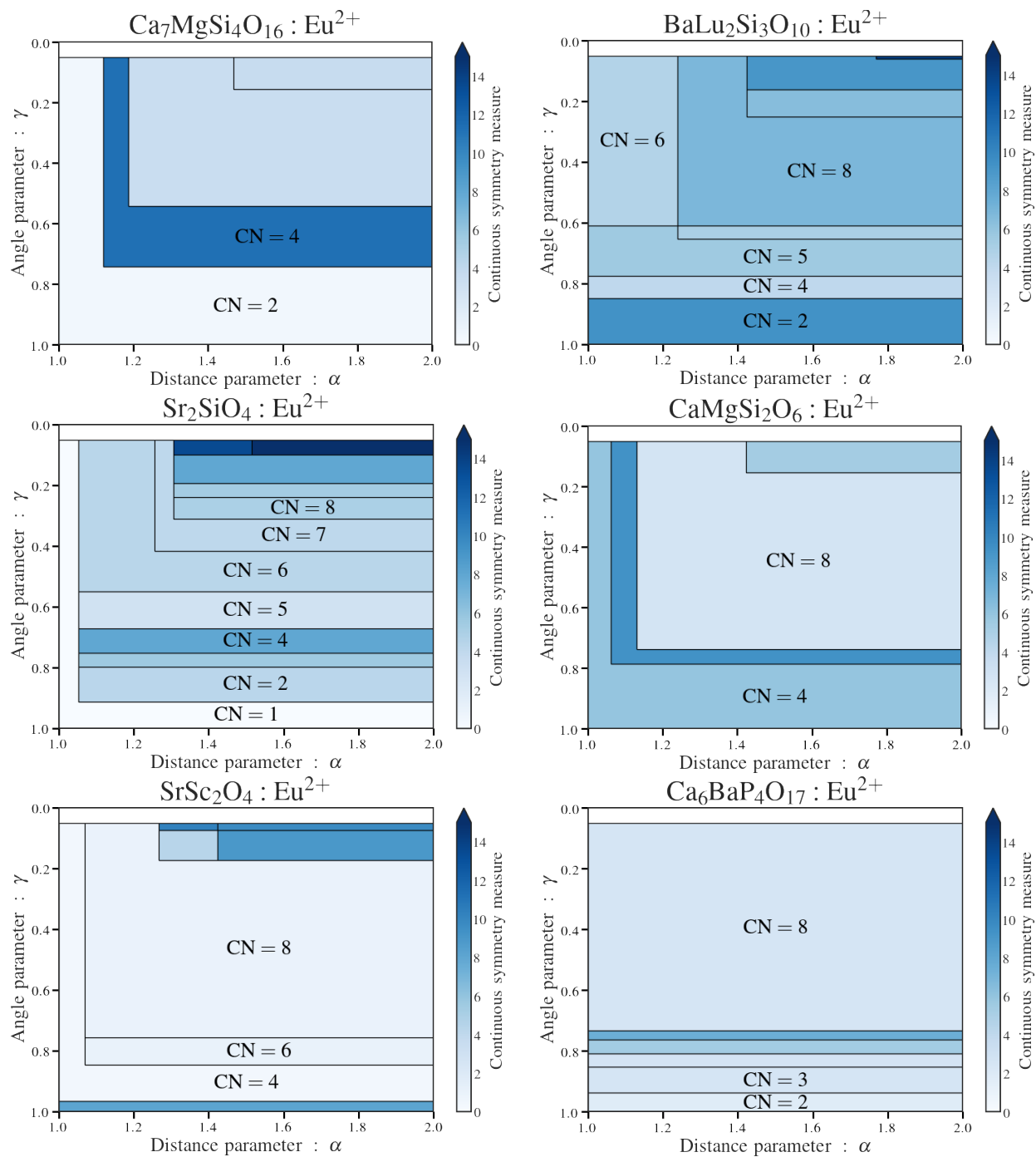


Figure S7. The Voronoi grid representation of Eu^{2+} local environment of all Eu^{2+} -activated hosts in Table S1.

References

- (1) Ronda, C. R. *Emission and Excitation Mechanisms of Phosphors*; 2007. <https://doi.org/10.1002/9783527621064.ch1>.
- (2) Dorenbos, P. Thermal Quenching of Eu^{2+} 5d–4f Luminescence in Inorganic Compounds. *Journal of Physics: Condensed Matter* **2005**, *17* (50), 8103–8111. <https://doi.org/10.1088/0953-8984/17/50/027>.
- (3) Ueda, J.; Dorenbos, P.; Bos, A. J. J.; Meijerink, A.; Tanabe, S. Insight into the Thermal Quenching Mechanism for $\text{Y}_3\text{Al}_5\text{O}_{12}:\text{Ce}^{3+}$ through Thermoluminescence Excitation Spectroscopy. *The Journal of Physical Chemistry C* **2015**, *119* (44), 25003–25008. <https://doi.org/10.1021/acs.jpcc.5b08828>.
- (4) Dorenbos, P. A Review on How Lanthanide Impurity Levels Change with Chemistry and Structure of Inorganic Compounds. *ECS J. Solid State Sci. Technol.* **2013**, *2* (2), R3001–R3011. <https://doi.org/10.1149/2.001302jss>.
- (5) Wang, Z.; Chu, I.-H.; Zhou, F.; Ong, S. P. Electronic Structure Descriptor for the Discovery of Narrow-Band Red-Emitting Phosphors. *Chemistry of Materials* **2016**, *28* (11), 4024–4031. <https://doi.org/10.1021/acs.chemmater.6b01496>.
- (6) Dorenbos, P. Relating the Energy of the $[\text{Xe}]5d^1$ Configuration of Ce^{3+} in Inorganic Compounds with Anion Polarizability and Cation Electronegativity. *Phys. Rev. B* **2002**, *65* (23), 235110. <https://doi.org/10.1103/PhysRevB.65.235110>.
- (7) Jones E, Oliphant E, Peterson P. *SciPy: Open Source Scientific Tools for Python*; 2001.
- (8) Park, K.; Kim, T.; Yu, Y.; Seo, K.; Kim, J. Y/Gd-Free Yellow $\text{Lu}_3\text{Al}_5\text{O}_{12}:\text{Ce}^{3+}$ Phosphor for White LEDs. *Journal of Luminescence* **2016**, *173*, 159–164. <https://doi.org/10.1016/j.jlumin.2016.01.014>.
- (9) Xu, J.; Chen, W.; Zeng, R.; Peng, D. A Carbon-Free Sol-Gel Method for Preparation of $\text{Lu}_3\text{Al}_5\text{O}_{12}:\text{Ce}^{3+}$ Phosphors for Potential Applications in Laser Scintillators and LEDs. *Materials Letters* **2014**, *133*, 1–4. <https://doi.org/10.1016/j.matlet.2014.06.030>.
- (10) Liu, Y.; Silver, J.; Xie, R.-J.; Zhang, J.; Xu, H.; Shao, H.; Jiang, J.; Jiang, H. An Excellent Cyan-Emitting Orthosilicate Phosphor for NUV-Pumped White LED Application. *Journal of Materials Chemistry C* **2017**, *5* (47), 12365–12377. <https://doi.org/10.1039/C7TC04168C>.
- (11) Bachmann, V. M. Temperature Quenching of the Yellow Ce^{3+} Luminescence in YAG:Ce. **2009**, *126* (9), 87–106.
- (12) Chen, L.; Lin, C. C.; Yeh, C. W.; Liu, R. S. Light Converting Inorganic Phosphors for White Light-Emitting Diodes. *Materials* **2010**, *3* (3), 2172–2195. <https://doi.org/10.3390/ma3032172>.
- (13) Akai, T.; Shigeiwa, M.; Okamoto, K.; Shimomura, Y.; Kijima, N.; Honma, T. XAFS Analysis of Local Structure around Ce in $\text{Ca}_3\text{Sc}_2\text{Si}_3\text{O}_{12}:\text{Ce}$ Phosphor for White LEDs. *AIP Conference Proceedings* **2007**, *882* (2007), 389–391. <https://doi.org/10.1063/1.2644534>.
- (14) Shimomura, Y.; Honma, T.; Shigeiwa, M.; Akai, T.; Okamoto, K.; Kijima, N. Photoluminescence and Crystal Structure of Green-Emitting $\text{Ca}_3\text{Sc}_2\text{Si}_3\text{O}_{12}:\text{Ce}^{3+}$ Phosphor for White Light Emitting Diodes. *Journal of The Electrochemical Society* **2007**, *154* (1), J35. <https://doi.org/10.1149/1.2388856>.
- (15) I. Levchuk, F. Schröppel, L. Römling, A. Osvet, N. Khaidukov, Y. Zorenko, R. Van Deun, M. Batentschuk, C. J. B. Highly luminescent $\text{Ca}_3\text{Sc}_2\text{Si}_3\text{O}_{12}:\text{Ce}^{3+}$ silicate garnet nano- and microparticles with 50–70% photoluminescence quantum yields as efficient phosphor converters for white LEDs https://www.techconnectworld.com/World2017/sym/Photonic_Materials_Devices.html.
- (16) Brgoch, J.; Borg, C. K. H.; Denault, K. A.; Mikhailovsky, A.; Denbaars, S. P.; Seshadri, R. An Efficient, Thermally Stable Cerium-Based Silicate Phosphor for Solid State White Lighting. *Inorganic Chemistry* **2013**, *52* (14), 8010–8016. <https://doi.org/10.1021/ic400614r>.
- (17) Li, K.; Liang, S.; Lian, H.; Shang, M.; Xing, B.; Lin, J. Ce^{3+} and Tb^{3+} -Doped Lutetium-Containing Silicate Phosphors: Synthesis, Structure Refinement and Photoluminescence Properties. *Journal of Materials Chemistry C* **2016**, *4* (16), 3443–3453. <https://doi.org/10.1039/c6tc00579a>.
- (18) Hermus, M.; Phan, P.-C.; Brgoch, J. Ab Initio Structure Determination and Photoluminescent Properties of an Efficient, Thermally Stable Blue Phosphor, $\text{Ba}_2\text{Y}_5\text{B}_5\text{O}_{17}:\text{Ce}^{3+}$. *Chem. Mater.* **2016**, *28* (4), 1121–1127. <https://doi.org/10.1021/acs.chemmater.5b04542>.
- (19) Katelnikovas, A.; Bettentrup, H.; Uhlich, D.; Sakirzanovas, S.; Jüstel, T.; Kareiva, A. Synthesis and Optical Properties of Ce^{3+} -Doped $\text{Y}_3\text{Mg}_2\text{AlSi}_2\text{O}_{12}$ Phosphors. *Journal of Luminescence* **2009**, *129* (11), 1356–1361. <https://doi.org/10.1016/j.jlumin.2009.07.006>.
- (20) Ogieglo, J. M.; Zych, A.; Ivanovskikh, K. V.; Jüstel, T.; Ronda, C. R.; Meijerink, A. Luminescence and Energy Transfer in $\text{Lu}_3\text{Al}_5\text{O}_{12}$ Scintillators Co-Doped with Ce^{3+} and Tb^{3+} . *The Journal of Physical Chemistry A* **2012**, *116* (33), 8464–8474. <https://doi.org/10.1021/jp301337f>.
- (21) Duke, A. C.; Hariyani, S.; Brgoch, J. $\text{Ba}_3\text{Y}_2\text{B}_6\text{O}_{15}:\text{Ce}^{3+}$ —A High Symmetry, Narrow-Emitting Blue Phosphor for Wide-Gamut White Lighting. *Chem. Mater.* **2018**, *30* (8), 2668–2675. <https://doi.org/10.1021/acs.chemmater.8b00111>.
- (22) Qiao, J.; Amachraa, M.; Molokeev, M.; Chuang, Y.-C.; Ong, S. P.; Zhang, Q.; Xia, Z. Engineering of $\text{K}_3\text{YSi}_2\text{O}_7$ To Tune Photoluminescence with Selected Activators and Site Occupancy. *Chem. Mater.* **2019**. <https://doi.org/10.1021/acs.chemmater.9b02990>.
- (23) Onuma, H.; Student, S. I. D.; Carpio, C. A. Del. Host Emission from $\text{BaMgAl}_{10}\text{O}_{17}$ and $\text{SrMgAl}_{10}\text{O}_{17}$ Phosphor : **2010**, 211–222.
- (24) Wang, L.; Zhang, H.; Li, Y.; Liang, P.; Shen, Y.; Jiao, F. Enhanced Luminescence in the $\text{SrMgAl}_{10}\text{O}_{17}:\text{Eu}^{2+}$ Blue Phosphor Prepared by a Hybrid Urea-Sol Combustion Route. *International Journal of Applied Ceramic Technology* **2016**, *13* (1), 185–190. <https://doi.org/10.1111/ijac.12420>.
- (25) Tang, Y. S.; Hu, S. F.; Lin, C. C.; Bagkar, N. C.; Liu, R. S. Thermally Stable Luminescence of $\text{KSrPO}_4:\text{Eu}^{2+}$ Phosphor for White Light UV Light-Emitting Diodes. *Applied Physics Letters* **2007**, *90* (15), 4–6. <https://doi.org/10.1063/1.2721846>.
- (26) Lin, C. C.; Xiao, Z. R.; Guo, G.-Y.; Chan, T.-S.; Liu, R.-S. Versatile Phosphate Phosphors ABPO_4 in White Light-Emitting Diodes: Collocated Characteristic Analysis and Theoretical Calculations. *Journal of The American Chemical Society* **2010**, *132* (9), 3020–3028. <https://doi.org/10.1021/ja9092456>.
- (27) Zhang, S.; Nakai, Y.; Tsuboi, T.; Huang, Y.; Seo, H. J. The Thermal Stabilities of Luminescence and Microstructures of Eu^{2+} -Doped KBaPO_4 and NaSrPO_4 with $\beta\text{-K}_2\text{SO}_4$ Type Structure. *Inorg. Chem.* **2011**, *50* (7), 2897–2904. <https://doi.org/10.1021/ic102504x>.
- (28) Wang, Z.; Ha, J.; Kim, Y. H.; Im, W. B.; McKittrick, J.; Ong, S. P. Mining Unexplored Chemistries for Phosphors for High-Color-Quality White-Light-Emitting Diodes. *Joule* **2018**, *2* (5), 914–926. <https://doi.org/10.1016/j.joule.2018.01.015>.
- (29) Wang, D. Y.; Huang, C. H.; Wu, Y. C.; Chen, T. M. $\text{BaZrSi}_3\text{O}_9:\text{Eu}^{2+}$: A Cyan-Emitting Phosphor with High Quantum Efficiency for White Light-Emitting Diodes. *Journal of Materials Chemistry* **2011**, *21* (29), 10818–10822. <https://doi.org/10.1039/c1jm00080b>.
- (30) Komukai, T.; Takatsuka, Y.; Kato, H.; Kakihana, M. Luminescence Properties of $\text{BaZrSi}_3\text{O}_9:\text{Eu}$ Synthesized by an Aqueous Solution Method. *Journal of Luminescence* **2015**, *158*, 328–332. <https://doi.org/10.1016/j.jlumin.2014.10.021>.
- (31) Brgoch, J.; Hasz, K.; Denault, K. A.; Borg, C. K. H.; Mikhailovsky, A. A.; Seshadri, R. Data-Driven Discovery of Energy Materials: Efficient $\text{BaM}_2\text{Si}_3\text{O}_{10}:\text{Eu}^{2+}$ ($M = \text{Sc}, \text{Lu}$) Phosphors for Application in Solid State White Lighting. *Faraday Discussions* **2014**, *176*, 333–347. <https://doi.org/10.1039/c4fd00125g>.
- (32) Kang, E.-H.; Choi, S.-W.; Chung, S. E.; Jang, J.; Kwon, S.; Hong, S.-H. Photoluminescence Characteristics of $\text{Sr}_3\text{SiO}_5:\text{Eu}^{2+}$ Yellow Phosphors Synthesized by Solid-State Method and Pechini Process. *Journal of The Electrochemical Society* **2011**, *158* (11), J330–J330. <https://doi.org/10.1149/2.016111jes>.
- (33) Li, Y.; Li, B.; Ni, C.; Yuan, S.; Wang, J.; Tang, Q.; Su, Q. Synthesis, Persistent Luminescence, and Thermoluminescence Properties of Yellow $\text{Sr}_3\text{SiO}_5:\text{Eu}^{2+}, \text{RE}^{3+}$ ($\text{RE} = \text{Ce}, \text{Nd}, \text{Dy}, \text{Ho}, \text{Er}, \text{Tm}, \text{Yb}$) and Orange-Red $\text{Sr}_{3-x}\text{Ba}_x\text{SiO}_5:\text{Eu}^{2+}, \text{Dy}^{3+}$. *Chemistry - An Asian Journal* **2014**, *9* (2), 494–499. <https://doi.org/10.1002/asia.201301045>.
- (34) Shao, Q.; Lin, H.; Dong, Y.; Fu, Y.; Liang, C.; He, J.; Jiang, J. Thermostability and Photostability of $\text{Sr}_3\text{SiO}_5:\text{Eu}^{2+}$ Phosphors for White LED Applications. *Journal of Solid State Chemistry* **2015**, *225*, 72–77. <https://doi.org/10.1016/j.jssc.2014.12.005>.

- (35) Zhang, X.; Zhang, J.; Wang, R.; Gong, M. Photo-Physical Behaviors of Efficient Green Phosphor $\text{Ba}_2\text{MgSi}_2\text{O}_7:\text{Eu}^{2+}$ and Its Application in Light-Emitting Diodes. *Journal of the American Ceramic Society* **2010**, *93* (5), 1368–1371. <https://doi.org/10.1111/j.1551-2916.2009.03549.x>.
- (36) Kim, J. S.; Park, Y. H.; Kim, S. M.; Choi, J. C.; Park, H. L. Temperature-Dependent Emission Spectra of $\text{M}_2\text{SiO}_4:\text{Eu}^{2+}$ (M=Ca, Sr, Ba) Phosphors for Green and Greenish White LEDs. *Solid State Communications* **2005**, *133* (7), 445–448. <https://doi.org/10.1016/j.ssc.2004.12.002>.
- (37) Brgoch, J.; Hasz, K.; Denault, K. A.; Borg, C. K. H.; Mikhailovsky, A. A.; Seshadri, R. Data-Driven Discovery of Energy Materials: Efficient $\text{BaM}_2\text{Si}_3\text{O}_{10}:\text{Eu}^{2+}$ (M = Sc, Lu) Phosphors for Application in Solid State White Lighting. *Faraday Discussions* **2014**, *176*, 333–347. <https://doi.org/10.1039/c4fd00125g>.
- (38) Li, Y. Q.; Hirosaki, N.; Xie, R. J.; Mitomo, M. Crystal, Electronic and Luminescence Properties of Eu^{2+} -Doped $\text{Sr}_2\text{Al}_{2-x}\text{Si}_{1+x}\text{O}_7-x\text{N}_x$. *Science and Technology of Advanced Materials* **2007**, *8* (7–8), 607–616. <https://doi.org/10.1016/j.stam.2007.08.007>.
- (39) Lu, F.-C.; Bai, L.-J.; Dang, W.; Yang, Z.-P.; Lin, P. Structure and Photoluminescence of Eu^{2+} Doped $\text{Sr}_2\text{Al}_2\text{SiO}_7$ Cyan-Green Emitting Phosphors. *ECS Journal of Solid State Science and Technology* **2014**, *4* (2), R27–R30. <https://doi.org/10.1149/2.0151502jss>.
- (40) Zhou, W.; Ma, X.; Zhang, M.; Luo, Y.; Xia, Z. Effect of Different RE Dopants on Phosphorescence Properties of $\text{Sr}_2\text{Al}_2\text{SiO}_7:\text{Eu}^{2+}$ Phosphors. *Journal of Rare Earths* **2015**, *33* (7), 700–705. [https://doi.org/10.1016/S1002-0721\(14\)60473-7](https://doi.org/10.1016/S1002-0721(14)60473-7).
- (41) Komuro, N.; Mikami, M.; Shimomura, Y.; Bithell, E. G.; Cheetham, A. K. Synthesis, Structure and Optical Properties of Cerium-Doped Calcium Barium Phosphate-a Novel Blue-Green Phosphor for Solid-State Lighting. *Journal of Materials Chemistry C* **2015**, *3* (1), 204–210. <https://doi.org/10.1039/c4tc01835d>.
- (42) Ha, J.; Wang, Z.; Novitskaya, E.; Hirata, G. A.; Graeve, O. A.; Ong, S. P.; McKittrick, J. An Integrated First Principles and Experimental Investigation of the Relationship between Structural Rigidity and Quantum Efficiency in Phosphors for Solid State Lighting. *Journal of Luminescence* **2016**, *179*, 297–305. <https://doi.org/10.1016/j.jlumin.2016.07.006>.
- (43) Zhang, X.; Tang, X.; Zhang, J.; Wang, H.; Shi, J.; Gong, M. Luminescent Properties of $\text{Sr}_2\text{MgSi}_2\text{O}_7:\text{Eu}^{2+}$ as Blue Phosphor for NUV Light-Emitting Diodes. *Powder Technology* **2010**, *204* (2–3), 263–267. <https://doi.org/10.1016/j.powtec.2010.08.011>.
- (44) Müller, M.; Volhard, M. F.; Jüstel, T. Photoluminescence and Afterglow of Deep Red Emitting $\text{SrSc}_2\text{O}_4:\text{Eu}^{2+}$. *RSC Advances* **2016**, *6* (10), 8483–8488. <https://doi.org/10.1039/c5ra25686k>.